

DISENTANGLING THE CIRCUMNUCLEAR ENVIRONS OF CENTAURUS A: I. HIGH RESOLUTION MOLECULAR GAS IMAGING

D. ESPADA^{1,2,3}, S. MATSUSHITA¹, A. PECK^{4,5}, C. HENKEL⁶, D. IONO⁷, F. P. ISRAEL⁸, S. MULLER¹, G. PETITPAS⁵, Y. PIHLSTRÖM⁹, G. B. TAYLOR⁹, AND DINH-V-TRUNG^{1,10}

Draft version December 1, 2008

ABSTRACT

We present high resolution images of the ¹²CO(2–1) emission in the central 1′ (1 kpc) of NGC 5128 (Centaurus A), observed using the Submillimeter Array. We elucidate for the first time the distribution and kinematics of the molecular gas in this region with a resolution of 6″0 × 2″4 (100 pc × 40 pc). We spatially resolve the circumnuclear molecular gas in the inner 24″ × 12″ (400 pc × 200 pc), which is elongated along a position angle P.A. \simeq 155° and perpendicular to the radio/X-ray jet. The SE and NW components of the circumnuclear gas are connected to molecular gas found at larger radii. This gas appears as two parallel filaments at P.A. = 120°, which are coextensive with the long sides of the 3 kiloparsec parallelogram shape of the previously observed dust continuum, as well as ionized and pure rotational H₂ lines. Spatial and kinematical asymmetries are apparent in both the circumnuclear and outer gas, suggesting non-coplanar and/or non-circular motions. We extend to inner radii ($r < 200$ pc) previously studied warped disk models built to reproduce the central parallelogram-shaped structure. Adopting the warped disk model we would confirm a gap in emission between the radii $r = 200 - 800$ pc (12″–50″), as has been suggested previously. Although this model explains this prominent feature, however, our ¹²CO(2 – –1) observations show relevant deviations from this model. Namely, the physical connection between the circumnuclear gas and that at larger radii, brighter SE and NW sides on the parallelogram-shaped feature, and an outer curvature of its long sides. Overall it resembles more closely an S-shaped morphology, a trend that is also found in other molecular species. Hence, we explore qualitatively the possible contribution of a weak bi-symmetric potential which would naturally explain these peculiarities.

Subject headings: galaxies: elliptical and lenticulars, cD — galaxies: individual (NGC 5128) — galaxies: structure — galaxies: ISM

1. INTRODUCTION

Radio galaxies are radio-loud active galaxies, usually of elliptical type. Their large scale synchrotron jets are presumably powered by the accretion of gas onto supermassive black holes, which are fuelled by reservoirs of neutral and ionized gas in the host galaxy. Many of these radio galaxies possess dust lanes containing large amounts of the different components of the interstellar medium (e.g. Allen et al. 2002). Cold gas traced by CO rotational lines is seen in some of these galaxies, with double-horned line profiles suggesting rotating disks in their nuclear region (e.g. Leon et al. 2003; Lim et al. 2003). The origin of the cold gas in these galaxies is still debated but it may be the result of mergers with smaller gas rich galaxies.

Understanding the distribution, kinematics and phys-

ical conditions of the nuclear gas in radio galaxies is essential to constrain the properties of the central engines of the most powerful active galactic nuclei (AGN). Questions that need to be addressed include: What are the mechanisms that drive the gas from kiloparsec to parsec scales? What are the gas concentrations in the nuclear region? Are the collimated and relativistic jets linked somehow to the gas seen at large scales? Powerful radio sources are rare in the local Universe, and thus the lack of high resolution observations has prevented the systematic study of the properties of the molecular gas in their nuclear region.

Centaurus A (Cen A, NGC 5128) is by far the nearest and best studied radio galaxy and thus plays an important role in our understanding of this major class of active galaxies. At its distance of $D \sim 3.42$ Mpc (Ferrarese et al. 2007), 1′ is approximately only 1 kpc, thus provides a unique opportunity to study the nuclear molecular gas in extraordinary detail. Cen A is often considered to be the prototypical Fanaroff-Riley (FR) class I low-luminosity radio galaxy hosting a type 2 AGN according to unified schemes (Antonucci 1993). Table 1 contains a summary of the characteristics of this galaxy from recent literature. For a detailed and comprehensive review, refer to Israel (1998).

At optical wavelengths the most characteristic feature of the galaxy, other than its typical elliptical appearance, is the warped and almost edge-on dust lane located along the minor axis of the galaxy. This dust lane contains a large amount of atomic, molecular and ionized gas (Israel 1998). Atomic hydrogen emission follows the dust lane and extends further out, to a radius of at least 7 kpc, showing asymmetries that indicate that the outer parts

¹ Academia Sinica, Institute of Astronomy and Astrophysics, P.O. Box 23-141, Taipei 106, Taiwan.

² Harvard-Smithsonian Center for Astrophysics, 60 Garden St., Cambridge, MA 02138; despada@cfa.harvard.edu

³ Instituto de Astrofísica de Andalucía - CSIC, Apdo. 3004, 18080 Granada, Spain

⁴ Joint ALMA Office, Av. El Golf 40, Piso 18, Las Condes, Santiago, Chile

⁵ Harvard-Smithsonian Center for Astrophysics, Submillimeter Array, 645 North A‘ohoku Place, Hilo, HI 96720

⁶ Max-Planck-Institut für Radioastronomie, Auf dem Hügel 69, 53121 Bonn, Germany

⁷ National Astronomical Observatory of Japan, 2-21-1 Osawa, Mitaka, Tokyo 181-8588, Japan

⁸ Sterrewacht Leiden, Niels-Bohr-Weg 2, 2300 CA Leiden, The Netherlands

⁹ Department of Physics and Astronomy, MSC07 4220, University of New Mexico, Albuquerque, NM 87131. Also Adjunct Astronomers at the National Radio Astronomy Observatory

¹⁰ On leave from Institute of Physics, Vietnamese Academy of Science & Technology, 10, Daotan, BaDinh, Hanoi, Vietnam

are not well ordered (van Gorkom et al. 1990; Schiminovich et al. 1994). The central region of Cen A (from 3 kpc to sub-pc scale) is very complex. The most prominent components are described as follows:

i) A *disk-like structure associated with the dust lane* ($\sim 5'$, or 5 kpc) as observed in H α (e.g. Nicholson et al. 1992), NIR (Quillen et al. 1993), submillimeter continuum (e.g. Hawarden et al. 1993; Leeuw et al. 2002), CO lines (e.g. Phillips et al. 1987; Eckart et al. 1990a; Rydbeck et al. 1993; Liszt 2001) and mid-IR continuum (e.g. Mirabel et al. 1999; Quillen et al. 2006). A remarkably symmetric structure is found within this disk in the inner 3 kpc. This feature is distributed along the dust lane at a position angle of 120° , and is usually described as an *S-shaped* or a *parallelogram structure* (a rhomboid-like feature with long and short sides of length $130''$ and $50''$, respectively). The former description has been used for example for ISOCAM mid-IR (Mirabel et al. 1999), JCMT submm (e.g. Leeuw et al. 2002) and recent Spitzer/IRS H $_2$ S(0) 28 μm observations (Quillen et al. 2008). The latter description is used in Spitzer/IRAC (Quillen et al. 2006) and Spitzer/IRS mid-IR observations (Quillen et al. 2008) of the continuum, ionized gas emission such as [Ne II] 12.8 μm , [S III] 33.4 μm and [Si II] 34.8 μm and PAHs (polyaromatic hydrocarbons). However, the two nomenclatures refer to the same structure and imply that emission in some species are more prominent in the SE and NW of the long sides of the parallelogram structure. This parallelogram structure has been well modelled by Quillen et al. (2006) using a non-coplanar model with circular motions, a slightly modified version of the warped disk model based on Spitzer/IRAC data, but originally obtained from previous CO, near-IR (Quillen et al. 1992, 1993) and H α observations (Bland 1986; Bland et al. 1987; Nicholson et al. 1992). Alternatively, it has been proposed that the observed features could be due to a ring-like structure within a bar (Mirabel et al. 1999; Marconi et al. 2000), which would partially explain the S-shaped morphology of some species.

ii) A *rapidly rotating circumnuclear region* within the central few 100 pc ($6'' - 25''$) of the galaxy, as suggested from broad molecular lines (mainly CO, e.g. Israel et al. 1990, 1991; Israel 1992; Rydbeck et al. 1993). Although previous single dish CO observations lack the angular resolution to resolve the circumnuclear region and to separate it from the outer disk of Cen A, the spectra toward the center show a broad plateau between $300 \text{ km s}^{-1} < V < 800 \text{ km s}^{-1}$ that was interpreted to be a circumnuclear molecular disk with an extent of a few 100 pc (Israel et al. 1991; Rydbeck et al. 1993). This component is also indicated by mid-IR/submm emission (e.g. Hawarden et al. 1993; Mirabel et al. 1999) and Pa α emission (Schreier et al. 1998b; Marconi et al. 2000), but remained undetected in H α mainly due to extinction (e.g. Nicholson et al. 1992).

iii) A *nuclear disk* (~ 30 pc, or $2''$) containing ionized and molecular gas presumably feeding a nuclear massive object (e.g. Marconi et al. 2001, 2006). While ionized gas species show non-rotational motions and are likely related to the jets, the molecular hydrogen as traced by H $_2$ (J=1-0) S(1) seems to be well distributed within a disk-like structure (Neumayer et al. 2007). Cen A hosts a compact sub-pc sized nuclear radio continuum source

exhibiting notable intensity variations at radio, infrared and X-ray wavelengths, presumably powered by accretion events (Israel 1998; Israel et al. 2008).

iv) *Absorption lines* toward the central continuum source detected in H I (e.g. Roberts 1970; van der Hulst et al. 1983; Sarma et al. 2002) and molecular lines (e.g. Israel et al. 1990; Wiklind & Combes 1997; Eckart et al. 1999), which provide the possibility to study the properties of the atomic and molecular clouds along the line of sight.

Since Cen A is located in the southern hemisphere (Declination $\simeq -43^\circ$), high resolution mapping of CO lines was not feasible until the advent of the Submillimeter Array (SMA¹; Ho et al. 2004). Here we report the findings of our $^{12}\text{CO}(2-1)$ observations with the SMA of its nuclear region with a resolution of $6''.0 \times 2''.4$ (100×40 pc). We use these high resolution interferometric observations to reveal the morphology and kinematics of the circumnuclear and outer molecular gas, as well as to elucidate the connection between these two molecular gas components. Further goals are to study the connection between molecular gas, dust, ionized gas and jets, and the evaluation of a model that best reproduces the observed features.

The paper is organized as follows: We introduce our SMA $^{12}\text{CO}(2-1)$ observations and data reduction in § 2. In § 3 we focus on the identification of the different components and study their physical properties. Possible models that can reproduce the CO emission are evaluated in § 4. In § 5 we compare our data with those from other wavelengths using the wealth of information from previous studies in the literature. We discuss our results in § 6 and finally summarize our conclusions in § 7. In a companion paper (Espada et al. 2008), we study the properties of the SMA $^{12}\text{CO}(2-1)$ absorption spectrum toward the compact bright continuum as well as VLBA H I absorption lines against both the nucleus and the nuclear jet.

2. SMA $^{12}\text{CO}(2-1)$ OBSERVATIONS AND DATA REDUCTION

Cen A was observed at 1.3 mm using the SMA with 7 antennas on April 5, 2006. In Table 2, we summarize the main parameters of our interferometric observations. The digital correlator was configured with 3072 channels (2 GHz bandwidth), resulting in a velocity resolution of about 1 km s^{-1} . The receivers were tuned to the redshifted $^{12}\text{CO}(2-1)$ ($\nu_{\text{rest}} = 230.538 \text{ GHz}$) emission line in the upper sideband (USB), using $V_{\text{LSR}} = 550 \text{ km s}^{-1}$. Note that velocities are expressed throughout this paper with respect to the LSR using the radio convention. This setting allowed us to simultaneously obtain the $^{13}\text{CO}(2-1)$ ($\nu_{\text{rest}} = 220.397 \text{ GHz}$) and C $^{18}\text{O}(2-1)$ ($\nu_{\text{rest}} = 219.560 \text{ GHz}$) lines in the lower sideband (LSB). We used R.A. = $13^{\text{h}}25^{\text{m}}27^{\text{s}}.6$ and Dec. = $-43^\circ 01' 09''.0$ (J2000) as our phase center, which is $0''.2$ offset from the AGN position R.A. = $13^{\text{h}}25^{\text{m}}27^{\text{s}}.615$ and Dec. = $-43^\circ 01' 08''.805$ (J2000; Ma et al. 1998). The maximum elevation of the source at the SMA site is $\simeq 27^\circ$, forcing us to observe only under very stable atmospheric

¹ The Submillimeter Array is a joint project between the Smithsonian Astrophysical Observatory and the Academia Sinica Institute of Astronomy and Astrophysics, and is funded by the Smithsonian Institution and the Academia Sinica.

conditions, with zenith opacities of typically $\tau_{225} \sim 0.10$. In order to have a beam shape as close to circular as possible we used a compact configuration with longer N–S baselines. Unprojected baseline lengths spanned 16 – 70 m, corresponding to 6 – 30 m projected baselines.

The editing and calibration of the data were done with the SMA-adapted MIR software². Callisto and 3C273 were used for passband calibration. An initial gain calibration was performed using J1316–3338, which is at an angular distance of 9° from the target. The continuum emission toward Cen A was found to consist of an unresolved source at its center. The gain calibration was thus refined using the averaged line-free channels in Cen A itself. 3C273 was used as absolute flux calibrator. Although this source is variable, it is frequently monitored at the SMA, and we adopted the value of 11.4 ± 0.8 Jy measured at 1 mm on 13 April, 2006. Overall, we estimate the absolute flux uncertainties on the order of 20%.

The imaging of the $^{12}\text{CO}(2-1)$ line was conducted in MIRIAD (Sault et al. 1995). A careful subtraction of the continuum was done using line-free channels with the task UVLIN. Since the continuum emission is so strong in this source, we paid special attention that continuum subtraction was done correctly by checking for possible artifacts in the line-free channels. The data were CLEANed with uniform weighting. This weighting was used to minimize the sidelobe level rather than the noise. Minimizing the sidelobe level is especially important in the N–S direction for channels close to the systemic velocity, where confusion by emission from different components, as well as the absorption features, can be a major problem in the cleaning process. The field of view (F.O.V.) is characterized by a Half Power Beam Width (HPBW) of the primary beam of an SMA antenna of $52''$ (0.9 kpc), and the resolution by the final synthesized beam of $2''.4 \times 6''.0$ (40×100 pc) with a major axis P.A. = 0.2° . The mean rms noise level is 64 mJy beam⁻¹ for the uniformly weighted 10 km s⁻¹ CLEANed channel maps. The task MOMENT was used to calculate the $^{12}\text{CO}(2-1)$ integrated flux density distribution and the intensity-weighted velocity field distribution (clipped at 2 times the rms noise).

3. RESULTS

The 1.3 mm continuum source was characterized by a total flux of 5.9 ± 1.0 Jy and was found to be unresolved. The $^{12}\text{CO}(2-1)$ line was detected in emission and absorption, $^{13}\text{CO}(2-1)$ only in absorption and $\text{C}^{18}\text{O}(2-1)$ was not detected in either emission or absorption.

In Figure 1 we compare the $^{12}\text{CO}(2-1)$ profile of Israel (1992) using the Swedish-ESO Submillimetre Telescope (SEST) with our SMA $^{12}\text{CO}(2-1)$ profile obtained by convolving the data to the $23''$ HPBW of the SEST and extracting the profile at the phase center. The $^{12}\text{CO}(2-1)$ emission line shows a broad plateau and a narrow line, in agreement with previous single-dish observations (e.g. Israel et al. 1991). The total integrated intensity of the $^{12}\text{CO}(2-1)$ line as seen from our convolved maps is 1790 ± 70 Jy km s⁻¹, recovering around 85% of the total flux measured using the SEST (1890 Jy km s⁻¹; Israel 1992). This is well within the absolute flux calibration uncertainties. We do not miss a large fraction of

the emission as a result of the lack of short-spacings, but we find systematically lower flux densities in the narrow line component (velocity range close to the systemic velocity). This component might therefore correspond to extended emission that is being filtered out. In contrast, the broad plateau should correspond to a quite compact spatial component, since we recover all the flux.

In Figure 2 we show the channel maps covering the velocity interval from 320 to 810 km s⁻¹ in 10 km s⁻¹ bins. Figures 3 and 4 show the $^{12}\text{CO}(2-1)$ integrated intensity (primary beam corrected) and velocity field maps, respectively. Position–Velocity (P–V) diagrams along several cuts are shown in Figure 5. Figure 5 a) and b) show the P–V diagrams along P.A. = 120° , for two different offsets in declination at $-10''$ and $+10''$ with respect to the center of the map. Figure 5 c) and d) show the P–V diagrams along the P.A. = 135° and 155° , respectively.

From the $^{12}\text{CO}(2-1)$ emission distributions and kinematics, we are able to distinguish between three components: 1) the broad plateau, corresponding to emission within the plotted ellipse around the center of the galaxy, in the form of a rotating circumnuclear structure (as outlined in § 1, ii); 2) the narrow line component, along the two parallel lines plotted from SE to NW with a P.A. = 120° and offset from the center at Dec. = $-10''$ and $+10''$, associated to the dust lane (gas at larger radii from the center, § 1, i); and 3) the absorption features toward the unresolved compact continuum component located in the galactic center (§ 1, iv), which will be described in a forthcoming paper (Espada et al. 2008). With our resolution, we are not able to resolve the nuclear disk (§ 1, iii).

In the following, we describe the observed broad plateau and narrow line components in more detail. A summary of the derived parameters for the $^{12}\text{CO}(2-1)$ emission for each component is shown in Table 3, including the peak flux density, mean velocity, velocity width and the total flux density ($S_{\text{CO}(2-1)}$).

3.1. Broad Plateau: Rapidly rotating circumnuclear gas

The $^{12}\text{CO}(2-1)$ channel maps (Figure 2) clearly show highly blueshifted ($\sim 340 - 420$ km s⁻¹) emission in the SE side of the AGN location and redshifted ($\sim 660 - 760$ km s⁻¹) emission on the NW side. This velocity range corresponds to the broad component of the spectrum that has a full width to zero power of $\Delta V \simeq 420 \pm 14$ km s⁻¹, spanning from 340 to 760 km s⁻¹ (Figure 1). The total integrated intensity and velocity field maps (Figure 3 and 4) show that this broad line plateau is located within the overlaid ellipse. The major and minor axes of this ellipse have lengths of $24'' \times 12''$ (400 pc \times 200 pc in linear scale without taking into account any projection effect) with a P.A. = 155° , centered on the AGN. The P–V diagram along the major axis of this ellipse (Figure 5 d) shows a gradient of 19.2 km s⁻¹ arcsec⁻¹ (or 1.2 km s⁻¹ pc⁻¹), which can be explained either by a disk or ring-like structure. Given that this broad line component is located exclusively in the inner $24''$ (400 pc), it must arise from an extended circumnuclear region. Although the emission is barely resolved in the N–S direction due to the elongated beam, the assumption of a (to first order) circular disk would imply that we are viewing the molecular component at an inclination angle of at least $i = 70^\circ$.

² MIR is a software package to reduce SMA data based on the package originally developed by Nick Scoville at Caltech. See <http://cfa-www.harvard.edu/~cqi/mircook.html>

3.2. Narrow Line: Gas at larger radii associated with the dust lane

The channel maps (Figure 2) also show emission, distributed along two parallel filaments ($\pm 10''$ north and south of the nucleus) with P.A. $\simeq 120^\circ$, from the SE edge of the F.O.V. at velocities $V = 430 \text{ km s}^{-1}$, up to the NW edge with $V = 650 \text{ km s}^{-1}$. These features correspond to the narrow ($\sim 100 \text{ km s}^{-1}$) line component previously observed in single-dish CO spectra (Figure 1; see also e.g. Israel et al. 1990). The P.A. of the circumnuclear gas and that of this component differ by $\Delta\text{P.A.} \simeq 35^\circ$. The two parallel features can be seen more clearly in the integrated intensity map (Figure 3). The velocity gradient of both of these two parallel features (Figures 4 and 5 a, b) is $3.2 \text{ km s}^{-1} \text{ arcsec}^{-1}$, which is 6 times smaller than that of the circumnuclear gas. The two (northern and southern) parallel features are quite similar in distribution and kinematics and must be somehow related to each other. In a zeroth-order approximation, both features would be in agreement with a highly inclined rotating ring located at a much larger radius than that of the circumnuclear gas, for which we only see the central $\sim 60''$ due to the restricted F.O.V. of our observations, at 230 GHz. However, the molecular gas is likely characterized by non-coplanar and/or non-circular motions, as explained in § 3.3.

3.3. Warped and/or Non-Circular Motions

We confirm from our $^{12}\text{CO}(2-1)$ data that the molecular gas is likely non-coplanar and/or contains non-circular motions. Evidence is summarized as follows: i) Large scale warp or non-circular motions in the gas at large radii: if emission arises from a coplanar (ring-like) feature, the connecting lines between the two lumps in each channel map (Figure 2, for example in channels $570 - 630 \text{ km s}^{-1}$) should be perpendicular to the major axis at P.A. = 120° . However we find an apparent misalignment. This can also be seen in the velocity field (Figure 4). Moreover, in channels within the $450 - 500 \text{ km s}^{-1}$ range in Figure 2 the northern lump seems to be superposed on the southern filament. ii) Brighter emission on the SE and NW sides in the two parallel filaments: on the receding side there is more emission in the northern filament than in the southern one, while the opposite is found on the approaching side (Figure 3). iii) Outer curvature: the emission does not exactly follow the drawn lines (Figure 3), but there is a curvature as we go farther from the centre. iv) Connections between circumnuclear and outer gas: are found in the range $V = 480 - 570 \text{ km s}^{-1}$ in the channel maps (Figure 2). The smooth connection of the gas kinematics in the SE between both components can be seen in the P-V diagram at angular offsets $8'' - 12''$ along P.A. = 135° and 155° (Figures 5 c and d). v) Warp and/or non-circular motions in the circumnuclear gas: although the high-velocity parts ($|V - V_{sys}| > 150 \text{ km s}^{-1}$, where V_{sys} is the systemic velocity) are quite symmetric and well centered kinematically, there are obvious deviations from co-planar and/or circular motions in the circumnuclear region at velocities close to V_{sys} . Whereas the receding part ($V = 620 - 680 \text{ km s}^{-1}$) is quite similar to a disk-like feature, the approaching side ($V = 420 - 480 \text{ km s}^{-1}$) is not, with more emission located in the eastern side of the

ellipse than in the region closer to the AGN.

Given the complexity of the circumnuclear region, we plot in Figure 6 a grid of emission line profiles. We discern the double-peaked profiles in the intersection regions between the circumnuclear and outer gas. We find velocity dispersions of about $\sigma = 50 - 60 \text{ km s}^{-1}$ (corresponding to a full width half maximum FWHM = $110 - 130 \text{ km s}^{-1}$) in the circumnuclear gas, which may be due to larger velocity gradients. The velocity dispersion in the molecular gas associated with the dust lane is 5 times smaller. The concentration of the circumnuclear gas peaks close to these intersection points. This double-peaked distribution in the circumnuclear gas may be similar to the twin peak feature often seen in the central region of barred galaxies (e.g. Kenney et al. 1992; Kohno et al. 1999). A caveat to the interpretation of the twin peak feature is the presence of a strong absorption line. Indeed, emission is seen to weaken in the inner regions from $V = 500$ to 600 km s^{-1} , but this can be explained only in part by the absorption features located on the red-shifted side ($V = 544 - 615 \text{ km s}^{-1}$) of the V_{sys} of Cen A (Espada et al. 2008). Therefore the twin peak interpretation is plausible. Moreover, the connection between the circumnuclear and outer gas found in the P-V diagram in the SE (Figures 5 c and d) reinforce this idea.

Note that the superposition of emission arising from the circumnuclear gas and that from the gas at larger radii causes a biased first moment. This is because the central value of the fit shifts as the relative prominence of the lines changes. For that reason we do not derive any values of velocities or widths from moment data. Nevertheless, Figure 4 is relevant since it illustrates the clear trend of rotation apparent in the circumnuclear gas.

3.4. Molecular Gas Mass

We separate the emission of the circumnuclear molecular gas from the molecular gas at larger radii in order to estimate their respective masses. We report in Table 3 the calculated molecular gas masses (M_{H_2}) of both components. For the circumnuclear molecular gas mass we take into account a conversion factor between integrated CO intensity and H_2 column density $X = N_{\text{H}_2}/I_{\text{CO}} = 0.4 \times 10^{20} \text{ cm}^{-2} (\text{K km s}^{-1})^{-1}$, which is a typical value observed in the nuclear regions of galaxies (Maloney & Black 1988; Wilson 1995; Mauersberger et al. 1996; Weiß et al. 2001). For the gas at larger radii, we adopt instead $X = 2.0 \times 10^{20} \text{ cm}^{-2} (\text{K km s}^{-1})^{-1}$, which is a mean value for $|b| < 5^\circ$ in the Galaxy (Dame et al. 2001). The conversion factor X may be uncertain by a factor of two even if Cen A were a spiral galaxy. Since the assumption of Cen A being a spiral obviously fails, a systematic error to X may be present which cannot be evaluated due to a lack of statistically relevant observational data. We also use a line ratio between $^{12}\text{CO}(1-0)$ and $(2-1)$ lines over the whole molecular disk of Cen A of $T_{\text{CO}(2-1)}/T_{\text{CO}(1-0)} \simeq 0.9$ (Rydbeck et al. 1993), and accounting for the ν^2 factor when converting flux densities to line temperatures. The integrated intensity of the circumnuclear gas is reduced by only about 2% of its total flux by the absorption line ($\int S dV = 25.6 \pm 0.5 \text{ Jy beam}^{-1} \text{ km s}^{-1}$, Espada et al. 2008), and therefore does not significantly affect our mass estimate.

We find the molecular gas masses of the circumnuclear gas and gas at larger radii to be $M_{\text{H}_2}^c = (0.6 \pm 0.1) \times 10^7 M_\odot$ and $M_{\text{H}_2}^o = (5.9 \pm 0.3) \times 10^7 M_\odot$, respectively, indicating that the outer component in our maps is about an order of magnitude as massive as the circumnuclear gas. We have detected a total molecular gas mass of $M_{\text{H}_2} \simeq (6.5 \pm 0.3) \times 10^7 M_\odot$. Note that errors do not include the uncertainties mainly arising from the X factor discussed above. The gas masses derived here can be re-scaled by a different conversion factor if a more appropriate value is found. Note that our maps (primary beam corrected) detect only a part of the narrow line component, so the true mass is larger than our estimate. From previously reported single-dish observations, the total $^{12}\text{CO}(1-0)$ luminosity is $L_{\text{CO}} = 10.8 \times 10^7 \text{ K km s}^{-1} \text{ pc}^2$ (Eckart et al. 1990b), which yields a molecular gas mass of $M_{\text{H}_2}^{\text{total}} \simeq 2.3 \times 10^8 M_\odot$, using $X = 2.0 \times 10^{20} \text{ cm}^{-2} (\text{K km s}^{-1})^{-1}$. Since the integrated flux density from the circumnuclear gas is just a small fraction of the total ($\sim 1/6$), the use of this conversion factor is a good estimate to derive the total gas mass. We therefore have in the region observed with the SMA ($52''$ HPBW) about 30 – 40 % of the total molecular gas mass.

The total gas mass in the inner $1'$ (1 kpc) is $M_{\text{gas}} \simeq (9.0 \pm 0.4) \times 10^7 M_\odot$ using $M_{\text{gas}} = 1.36 \times M_{\text{H}_2}$, where the factor 1.36 accounts for elements other than hydrogen (Allen 1973; Sakamoto et al. 1999). From that amount, there is $M_{\text{gas}}^c \simeq (0.8 \pm 0.1) \times 10^7 M_\odot$ in the inner projected distance $r < 200 \text{ pc}$ ($12''$). The surface density within $r = 200 \text{ pc}$ is $\Sigma_{\text{gas}, 200 \text{ pc}} \simeq 65 M_\odot \text{ pc}^{-2}$ assuming a disk-like feature with inclination $i = 70^\circ$. The dynamical mass within the circumnuclear gas can be calculated as $M_{\text{dyn}, 200 \text{ pc}} = r (V/\sin i)^2/G = 4.6 \times 10^9 M_\odot$, as obtained from the maximum rotational velocity $V \simeq 200 \text{ km s}^{-1}$ corrected for an inclination of $i = 70^\circ$. Thus the molecular gas in Cen A constitutes less than 2% of the dynamical total mass within the radius $r = 200 \text{ pc}$.

4. MODELS: WARPED THIN DISK, WEAK BAR AND COMBINED MODELS

There is evidence that the gas and dust are relatively well settled in the inner $5'$ (5 kpc) (e.g. Nicholson et al. 1992; Rydbeck et al. 1993; Quillen et al. 2006). Nicholson et al. (1992) and Quillen et al. (1992) have shown, with $\text{H}\alpha$ and CO respectively, that co-planar motions are not in agreement with the observations. Quillen et al. (2006) present a slightly revised version of a warped disk model using circular orbits, based on previous CO, near-IR (Quillen et al. 1992, 1993) and $\text{H}\alpha$ observations (Bland 1986; Bland et al. 1987; Nicholson et al. 1992), which successfully reproduce the observed parallelogram structure (Quillen et al. 2006).

Another proposed interpretation is an embedded large scale ($\sim 5'$, or 5 kpc) stellar bar structure (Mirabel et al. 1999, mid-IR), but analysis of the detailed applicability of this model has not been performed. One point against this interpretation is the fact that the total molecular gas mass accounts only for about 2% of the dynamical gas mass (§ 3.4) so the molecular gas motions are expected to be mainly dominated by the stellar component (and dark matter), but no non-axisymmetry of the stellar component has been seen or inferred from kinematic

observations or mass models of the central stellar region. Quillen et al. (2006) have also searched for evidence of a large-scale stellar bar in the isophote shapes $3.6 \mu\text{m}$ Spitzer/IRAC images, which is not affected by extinction, and obtained negative results. On the other hand, although a strong bar model can probably be discarded due to the lack of a prominent non-axisymmetric stellar component, it would still be difficult to detect a weak non-axisymmetric stellar component (such as that of a putative weak 'bar'), because the disk is nearly edge-on, masked by the dust lane, and embedded in the bright spheroidal component. Evidence for a nuclear bar has been suggested for example by Marconi et al. (2001), who find that VLT/ISAAC spectra along different P.A. in the central $25''$ of $\text{H}_2(\text{J}=1-0) \text{ S}(1)$ ($\sim 500 \text{ pc}$) is probably characterized by non-circular motions.

The lack of observations of the gas with sufficient spatial resolution from 100 pc to kiloparsec scale as well as kinematical information, in addition to high extinction ($A_V = 27 \pm 5 \text{ mag}$, Israel et al. 1990), has further limited our knowledge on boundary conditions that are essential to model the circumnuclear region of Cen A.

In this section, we investigate a comparison of our $^{12}\text{CO}(2-1)$ data (§ 3) with the revised warped disk model in Quillen et al. (2006). Encouraged by the observed deviations with respect to this model (§ 4.1), we propose that non-circular motions via a weak bi-symmetric potential may partly govern the distribution and kinematics of the molecular gas (§ 4.2 and § 4.3).

We have collated the available information of the line of sight velocities from different components of the ISM in order to estimate a generic rotation curve. Although the gas motion may be non-circular and/or not co-planar, a rough estimate of the rotation curve suffices for our qualitative modelling. The line of sight velocity data and the derived rotation curve are shown in Figure 7. Data for the line of sight velocities (indicated by cross signs) include $^{12}\text{CO}(2-1)$ from the circumnuclear gas up to a radius of 0.2 kpc (§ 3.1), $^{12}\text{CO}(2-1)$ of the gas at larger radii (§ 3.2), $\text{H}\alpha$ (Nicholson et al. 1992) and $^{12}\text{CO}(3-2)$ (Liszt 2001) (Table 4). The estimated rotation curve grows monotonically as $1.2 \text{ km s}^{-1} \text{ pc}^{-1}$ up to $r = 0.2 \text{ kpc}$ and flattens to $0.2 - 0.3 \text{ km s}^{-1} \text{ pc}^{-1}$ beyond 1 kpc.

4.1. Warped Disk Model

We use recent estimates of the inclination and P.A. for the different tilted rings with radii $r \geq 800 \text{ pc}$ ($50''$) from Quillen et al. (2006), and extend the model for inner radii $r < 200 \text{ pc}$ ($12''$) (circumnuclear molecular gas), where we use a P.A. $\sim 155^\circ$ and an inclination $i \sim 70^\circ$ as obtained in § 3.1. Originally the model by Quillen et al. (2006) assumes the existence of a circumnuclear disk within $r = 100 \text{ pc}$ ($6''$) (Marconi et al. 2001; Israel et al. 1991), and a gap beyond this circumnuclear disk out to a radius $r \simeq 800 \text{ pc}$ ($50''$), which is suggested by a comparison with their Spitzer/IRAC mid-IR images. Without this gap, the model would show a bright linear feature at $r < 1 \text{ kpc}$ ($1'$) within the parallel filaments (Quillen et al. 2006, their Fig. 10) that is not observed. The infrared surface distribution depends on the inclination of the disk, but other mapped species such as the $\text{Pa}\alpha$ (Marconi et al. 2000) and our $^{12}\text{CO}(2-1)$ emission show the same trend. Note that the ad-hoc physical gap used in this model implies that there is no physical con-

nection between the circumnuclear gas and the warped disk at larger radii.

In Figure 8 we show: a) the inclination and P.A. as a function of radius that properly reproduce the mid-IR emission, where it is assumed that there is a physical gap in the distribution within $200 \text{ pc} < r < 800 \text{ pc}$ ($6'' < r < 50''$); b) the projected circular orbits; c) the normalized intensity plot, as obtained from the projected orbit distribution; d) the velocity field map, taking into account the rotation curve in Figure 7; e) and f) the distribution and velocity field in the inner 1 kpc ($1'$).

From a comparison with our $^{12}\text{CO}(2-1)$ distribution and velocity field maps (Figure 3, 4), the overall distribution (parallelogram structure and circumnuclear gas) and kinematics seem to match well, with the circumnuclear gas showing a larger velocity gradient, and the outer gas with a smaller gradual change in velocity. However, a number of details found in our $^{12}\text{CO}(2-1)$ maps and indicated in § 3.3 are not well reproduced by this model, including: 1) a physical connection between the circumnuclear gas and that at larger radii, 2) brighter SE and NW sides on the parallelogram-shaped feature, and 3) an outer curvature of its long sides.

4.2. Co-planar Weak Bar Model

We inspect whether a disk perturbed by a weak bar potential can resemble the observed $^{12}\text{CO}(2-1)$ emission properties in the inner $\sim 1'$ (1 kpc). We use a damped orbit model as in Wada (1994) to describe gas motions in a weak bar potential within an axisymmetric potential and assuming epicyclic orbits. Note that this model is different to the strong stellar bar model (few kiloparsec scale) proposed for Cen A as suggested by Mirabel et al. (1999), where the observed features in Cen A are even compared to the prototypical barred galaxy NGC 1530. Because there is no evidence for a strong stellar potential in Cen A, the assumption that it has a strong bar like NGC 1530 may not be well justified. It is also different to the models used by Quillen et al. (1992), where non-circular motions within a coplanar disk are obtained as a result of a large triaxial stellar potential (i.e. a prolate/triaxial model with axis ratios 1:2:2.6). These do not reproduce their ^{12}CO observations at large scale (resolution of about $30''$ FWHM). We use instead a weak non-axisymmetric potential to model the gas only in the inner $\sim 1'$ (1 kpc), which has not been inspected to date for this source.

A schematic view of the (projected) features produced by the proposed weak bi-symmetric potential is shown in Figure 9, where all the components (circumnuclear gas $-x_2$ orbits-, as well as outer gas $-x_1$ orbits- that corresponds to the parallelogram structure) in the inner 3 kpc of the galaxy are shown. The fixed parameters of the weak bar model are: a rotation curve (to fit a given axisymmetric potential), a bar potential, inclination and P.A. for the gas disk, bar strength ϵ , bar pattern speed Ω_b and a damping parameter Λ . We use a conservative bar strength ($\epsilon = 0.03$) since there is no signature of a strong large stellar bar (Quillen et al. 2006). A larger ϵ would mainly produce a higher contrast between the circumnuclear disk and the outer regions. We estimate the pattern speed $\Omega_b = 0.3$ by assuming that the Inner Lindblad Resonance (ILR) is located where the circumnuclear gas runs out, at a radius of about $r_{\text{ILR}} = 0.2 \text{ kpc}$.

Then the Outer Inner Lindblad Resonance (OILR) would be at $r_{\text{OILR}} = 0.7 \text{ kpc}$, approximately at the location of the gas at larger radii. The damping parameter was fixed arbitrarily to $\Lambda = 0.1$, although that only affects the orientation of the x_1 and x_2 orbits (Wada 1994). We use the rotation curve data points in Figure 7 to obtain a fit (dashed line) using an axisymmetric logarithmic potential $\Phi_0(r) = 0.5 \times \log(a+r^2/b)$, with $a = 1.0$ and $b = 0.05$. We also show in Figure 7 the curves for Ω (solid line), κ (dotted line) and $\Omega \pm \frac{\kappa}{2}$ (dashed-dotted lines) as a function of radius. We inspect a weak bar model within a flat disk. In Figure 10 we show the following composition: Figure 10 a) the inclination and P.A., which in this case are kept constant at $i = 45^\circ$ and P.A. = 100° ; Figure 10 b) the damped orbits; Figure 10 c) and d) show the normalized intensity distribution and its corresponding velocity field; and finally a zoom of these maps to the inner kiloparsec in Figure 10 e) and f). Note that the inclination is set to a smaller value than its average $i \sim 70 - 80^\circ$ in order to illustrate the morphology of this model more clearly.

This model produces a disk-like feature with two arms, a large concentration at inner radii and a gap outside of these two structures, where the number of orbits is at a minimum. Although the NW and SE sections of the parallel filaments are brighter than the other two sides, the outer curvature and the connections between circumnuclear and outer gas could resemble the gas distribution and kinematics derived from our maps (§ 3.3), the assumption of a co-planar morphology is not sufficient to reproduce the observed parallelogram structure.

4.3. Combined Model: Weak Bar within a Warped Disk

Constraints to the inclination and position angle (from previous knowledge of the disk properties at larger scale) can be used in order to get a more accurate model based on a weak bar. The inclination with respect to the viewer must cross 90° (edge-on), from $i = 70^\circ$ inside $r < 200 \text{ pc}$ ($12''$) to $i = 70 - 80^\circ$ (but inverted orientation) at $r > 1 \text{ kpc}$ ($1'$) (e.g. Quillen et al. 2006, and § 5.4). In the present model the edge-on transition should take place where the lack of emission is more prominent in the pure bar model (§ 4.2), at $r \sim 600 \text{ pc}$ or $40''$, versus the 1 kpc or $60''$ of the warped disk model (§ 4.1). In addition, from our observations, the P.A. = 155° as observed in the circumnuclear gas ($r < 200 \text{ pc}$, or $12''$) and the P.A. = 120° in the molecular gas at larger radii ($r > 800 \text{ pc}$, or $> 50''$). We adopt these constraints to the weak bar model in § 4.2. Following the design of Figures 8 (§ 4.1) and 10 (§ 4.2), this combined model containing a simple warped model modified by a weak bar model is shown in Figure 11. Inclination and P.A. are detailed in Figure 11 a). The resulting projected orbits are plotted in Figure 11 b). The normalized intensity distribution and the velocity field images, as well as a zoom of these maps are plotted in Figure 11 c) – f).

This combined model shows some difference from the warped disk model due to the addition of the weak bar. We find two arms, a large concentration at inner radii and a region with a lack of emission outside of these two structures, as in § 4.2. The extra information of the weak bar model helps us to naturally explain the connection of circumnuclear and outer gas without contradicting the lack of emission along a preferential direction, as observed in

Figure 11 b), and in the normalized distributions in Figure 11 c) and e). In addition, the model's spiral arms follow the locations of relatively strong $^{12}\text{CO}(2-1)$ emission to the SE and NW of the center (brighter NW and SE regions). Also, the curvature of the molecular gas associated with the parallel lines (see for example Figure 3 and Figure 11 c) is reproduced in our model. On the other hand, a drawback to this model is that the velocity field does not show the large velocity gradient found in the intersections between the circumnuclear gas and the gas at larger radii.

At larger radii $r > 1$ kpc ($1'$), the inclination and P.A. of the rings should follow that of Quillen et al. (2006). Our observations can not provide relevant information at these larger scales (or smaller scale, such as the model proposed by Neumayer et al. 2007 for the very inner $3''$, or 50 pc).

5. COMPARISONS WITH PREVIOUS WORKS

There is a wealth of information available in the literature for Cen A. In the following we discuss our results in the context of previous work, emphasizing the molecular gas in the inner kiloparsec of the galaxy, but also taking into account other relevant information to trace the different phases of the ISM that are present in this region.

5.1. Molecular Gas

The main improvement of our SMA $^{12}\text{CO}(2-1)$ data over previous single-dish observations is our higher angular resolution, a factor of 45 in beam area with respect to the highest resolution $^{12}\text{CO}(2-1)$ maps previously obtained ($23''$ resolution or ~ 380 pc for $\text{CO}(2-1)$; Rydbeck et al. 1993). Therefore, our $^{12}\text{CO}(2-1)$ data allow us for the first time to distinguish between the different components (i.e. outer and circumnuclear molecular gas and absorption features) and to constrain models more accurately, especially in the interesting nuclear region.

The presence of the ‘‘circumnuclear disk or ring’’ (e.g. Israel et al. 1990, 1991; Rydbeck et al. 1993; Hawarden et al. 1993) can be clearly distinguished in our maps. This rapidly rotating compact feature was previously determined to have a radius of typically $\sim 100 - 300$ pc, with rotational velocities of ~ 175 km s^{-1} . The estimated extent of the inner disk given by Israel et al. (1991) from the broader component of the CO lines, $30''$ (or 500 pc), is larger than what we obtain. Rydbeck et al. (1993) suggested, using beam deconvolution of single-dish observations, that the broad component was in fact a 100 pc edge-on circumnuclear ring. The extent was therefore underestimated in this case. Rydbeck et al. (1993) suggested that the major axis of the circumnuclear gas has a P.A. $\sim 145^\circ$, close to our result P.A. = 155° .

Molecular hydrogen observations by Marconi et al. (2001) (slits along different P.A. using VLT/ISAAC, H_2 ($J=1-0$) $S(1)$ 2.122 μm) show the H_2 counterpart of our CO emission in the inner $r = 24''$ (~ 400 pc), including the slowly rotating contribution of the gas in the dust lane, a circumnuclear disk or ring ($\sim 6''$, or 100 pc) and the nuclear disk ($\sim 2''$, 30 pc). The different slits are remarkably similar to our P-V diagrams (especially that along P.A. = 135.5°). Neumayer et al. (2007) have imaged the same transition (H_2 ($J=1-0$) $S(1)$, 2.122 μm)

using VLT/SINFONI in the inner $3''$ (~ 50 pc). They show that is characterized by a mean inclination angle of 34° and a P.A. = 155° assuming a warped disk model to describe its gas kinematics. The inclination rises from 34.2° at $0''.76$ to $\sim 58.9^\circ$ at $1''.9$, and would probably continue rising to the $i \geq 70^\circ$ of our circumnuclear gas. Neumayer et al.'s model also suggests an average P.A. = 155° , which is the same as the P.A. of our $^{12}\text{CO}(2-1)$ circumnuclear gas. However, the possibility of non-circular motions at these scales has not been excluded.

At a larger scale, pure rotational lines of molecular hydrogen H_2 ($J=2-0$) $S(0)$ (28.22 μm) emission observed with Spitzer/IRS by Quillen et al. (2008) are remarkably similar to the ^{12}CO emission. Both are asymmetric with respect to the parallelogram structure, at least in the inner $45''$ (or 750 pc) (see their Figure 6), with the SE and NW sides of the parallelogram being brighter than the opposite two sides, as our $^{12}\text{CO}(2-1)$ maps. No explanation for this asymmetry was given by Quillen et al. (2008). A possible interpretation of this has been given in our weak bar within a warped disk model (§ 4.3). Since the molecular hydrogen transition H_2 ($J=2-0$) $S(0)$ indicates the presence of gas with $T \sim 200$ K (Quillen et al. 2008) along the S-shaped feature, our model suggests that this warm molecular gas would be preferentially located along the spiral arms where shocked regions are present. In this scenario the molecular gas would be heated by the abundant star formation and shocks that may take place in these regions.

5.2. Ionized gas

The star formation rate in the disk has been estimated to be about $\sim 1 M_\odot \text{ yr}^{-1}$, based on the infrared luminosity estimated by Eckart et al. (1990a). Marconi et al. (2000)'s HST/NICMOS observations in a $50'' \times 50''$ circumnuclear region suggest that the Pa α is located in a ring-like structure with higher star formation than the rest ($\sim 0.3 M_\odot \text{ yr}^{-1}$). The NW and SE sides of the parallelogram structure are brighter than their opposite sides in [Si II] (34.8 μm), [S III] (33.5 μm) and [Fe II] (25.988 μm) (Quillen et al. 2008), as previously mentioned for the molecular gas. These species likely trace HII regions. Other higher ionization tracers such as [O IV] (25.9 μm) and [Ne V] (24.3 μm) are distributed along the jet. This would be in agreement with non-rotational motions exhibited in the inner $3''$ in Br γ , [Fe II] and [Si IV] (Neumayer et al. 2007), and likely result from interaction of the gas with the jet.

The reason for the star formation regions not being equally distributed along the two parallel-shaped structure is still unknown. Variations in the brightness of star forming regions could be partly responsible for this effect, but since the molecular gas also shows the same trend, it may be more appropriate to suggest that these are in fact regions with larger amounts of gas and with enhanced star formation, probably as a result of shocks driven into the gas by the putative weak bar.

5.3. Dust Emission

We compare the distribution of the molecular gas as traced by the $^{12}\text{CO}(2-1)$ line to the dust emission. Resolutions spanning $3 - 6''$ are available in 5 $\mu\text{m} - 18$ μm ISOCAM images for the warm dust (including complex molecules) by Mirabel et al. (1999), covering a $2'$

field around the core. Best resolutions, of the order of $1'' - 2''$ over a $5' \times 5'$ region, have been recently obtained by Quillen et al. (2006) using Spitzer/IRAC in the $2 \mu\text{m} - 8 \mu\text{m}$ range. For the colder dust, $450 \mu\text{m}$ and $850 \mu\text{m}$ submillimeter observations have been obtained using SCUBA with HPBWs of $14''.5$ and $8''.0$ covering the central $450'' \times 100''$, respectively (Leeuw et al. 2002). While the $5 \mu\text{m} - 18 \mu\text{m}$ ISOCAM images and submm images show an S-shaped feature and an extension with P.A. = 145° in the inner $r = 15''$, the Spitzer/IRAC $2 \mu\text{m} - 8 \mu\text{m}$ images show a structure that looks like a parallelogram structure, without a clear extension to the nuclear region.

The warm dust and emission by complex molecules (PAHs) are well coupled to the CO(2-1) distribution, both show a similar structure, and even the main clumps are collocated. In Figure 12 we show an overlay of the mid-IR $8 \mu\text{m}$ image from Spitzer (Quillen et al. 2006) and our $^{12}\text{CO}(2-1)$ line distribution. The agreement between the mid-IR and CO line emission is excellent, except for the very center of the galaxy. The dust emission (as traced by mid-IR) seems to be depleted at intermediate radii: Quillen et al. (2006) proposed a gap from $6'' < r < 50''$ ($100 \text{ pc} < r < 800 \text{ pc}$) in order to match their optically thin warped disk model to the mid-IR emission. However, since the infrared surface brightness depends on the inclination of the disk, Quillen et al. (2006) noted that if the disk twists to lower inclinations at small radii it would have lower surface brightness near the nucleus. Nicholson et al. (1992) also suggest that there is a lack of emission in ionized gas within $60''$ although this could be partly caused by extinction. Assuming a warped disk model, our observations would confirm the existence of a gap between $200 < r < 800 \text{ pc}$ and a central concentration at $r < 200 \text{ pc}$ ($12''.5$). However, it would not explain the obvious physical connection between the circumnuclear gas and gas at larger radii, which would be more easily explained by the combined model (§ 4.3).

We show in Figure 13 the ratio of emission at mid-IR $8 \mu\text{m}$ (Quillen et al. 2006) and $^{12}\text{CO}(2-1)$ emission. It is observed that toward the center the ratio of $^{12}\text{CO}(2-1)$ emission to $8 \mu\text{m}$ is larger than in the outer regions. The observed gradient might be explained by temperature differences toward the center caused by winds and high-energy radiation from the AGN (Israel 1998 and references therein), as derived by: i) the very red near-IR colours within the inner $r = 200 \text{ pc}$ ($12''$), which cannot be explained just by extinction, but also need elevated dust temperatures, shocks and UV and X-ray radiation from the nucleus; and ii) the compactness of [Fe II], Pa α and H $_2$ emission, with extents of $\sim 40 \text{ pc}$ and rotating with 215 km s^{-1} at temperatures of $\sim 1000 \text{ K}$ and densities in excess of 10^5 cm^{-3} .

5.4. Geometrical Relation between Circumnuclear Gas and Nuclear Activity

A progression from the disk-like structure along the dust lane (few kpc scale) to the circumnuclear gas (few hundred pc scale) and then to the inner accretion disk (inner 10 pc) would be expected if this gas is indeed the fuel for the AGN. In this case the accretion disk might be expected to be oriented perpendicular to the jet. However, this has been the object of controversy

over the last two decades. While in spiral galaxies inner disks have a random orientation with respect to the large scale outer disks (Ulvestad & Wilson 1984), this is probably not the case in elliptical galaxies (Moellenhoff et al. 1992). However Schmitt et al. (2002) find that this correlation is not strong using three dimensional information. Recently Verdoes Kleijn & de Zeeuw (2005) have also shown, using three dimensional information, that the jet is approximately perpendicular to the dust structure in the galaxies possessing filamentary dust structures or dust lanes (only $\simeq 20^\circ$ misalignment angle, as is the case of Cen A), whereas galaxies having regular dust structures with an elliptical appearance have a much wider distribution ($\simeq 45^\circ$ misalignment angle).

To illustrate that the circumnuclear gas is indeed perpendicular to the inner jet as projected in the sky plane we show in Figure 12 a superposition of the 21 cm radio continuum image (Sarma et al. 2002) and our $^{12}\text{CO}(2-1)$ map. The relativistic jet is at a P.A. $\simeq 51^\circ$, which is nearly perpendicular in projection to the circumnuclear gas, P.A. $\simeq 155^\circ$. At an even smaller scale, the radio continuum emission at 2.3, 4.8, 8.4 and 22.2 GHz observed using the Southern Hemisphere VLBI and VLBA by Tingay et al. (1998), or even the space-VLBI at 4.9 GHz by Horiuchi et al. (2006), nicely show the same P.A. $\simeq 51^\circ$ for the nuclear jet. An X-ray jet is also reported to be coextensive at a similar P.A. (Kraft et al. 2002).

Information about the three dimensional geometry of the jet can be extracted from the difference in luminosity of the NE jet and the SW counter jet caused by the relativistic beaming effect and the motions and temporal variations in the jets. From Figure 12 b), it is clear that the NE inner jet is brighter than the SW counter jet and thus the former is likely pointing towards us. Tingay et al. (1998) conclude that the axis of the Cen A jet lies between $i \simeq 50^\circ$ and 80° to our line of sight. We derived an inclination for the circumnuclear gas of $i \geq 70^\circ$ (§ 3) if the near side is to the SW. If the nuclear jet happens to be perpendicular to the circumnuclear gas, an orientation of the nuclear jet with respect to the line of sight of $\simeq 50^\circ - 80^\circ$ (Tingay et al. 1998, using VLBI observations) would be compatible. This is in contrast to the results of Neumayer et al. (2007), whose mean inclination of the modelled warped disk is $i = 34^\circ$. This value is closer to the $20^\circ < i < 50^\circ$ found by Hardcastle et al. (2003) using VLA observations. The VLBI observations by Tingay et al. have much higher angular resolution and trace only the innermost region of the jet.

We can also estimate the time scale in which the observed amount of circumnuclear molecular gas will be consumed just by accretion with the current rate of energy emitted by the nucleus. The active nucleus is well below the Eddington luminosity (Marconi et al. 2001). The bolometric luminosity is estimated to be $L_{bol} \simeq 10^{43} \text{ erg s}^{-1}$, with half of it taking place at high energies (Israel 1998). With a typical efficiency from the total luminosity to mass accretion of 0.1, we obtain a mass accretion rate of $dM/dt \sim 2 \times 10^{-3} M_\odot \text{ yr}^{-1}$. With our derived total amount of molecular gas in the nuclear region $M_{gas}^c = (0.8 \pm 0.1) \times 10^7 M_\odot$ (with a conversion factor $X = 0.4 \text{ cm}^{-2} (\text{K km s}^{-1})^{-1}$), the time scale to consume it would be of the order of 1 Gyr. Note however that the Eddington luminosity estimated with a black hole

mass of $M_{BH} \simeq 10^{7-8} M_{\odot}$ (Marconi et al. 2001, 2006; Krajnović et al. 2007; Neumayer et al. 2007) is about 2–3 orders of magnitude larger than the measured L_{bol} . The entirety of the circumnuclear molecular gas would be consumed if the Eddington luminosity is maintained within a range of 10^{6-7} yr.

6. DISCUSSION

6.1. Warped Disk or Combined model?

The warped disk model is the preferred model to date. It has been used successfully to reproduce the observations both at a large scale (e.g. Quillen et al. 2006) and also at a few parsec scale (Neumayer et al. 2007). Our observations give information about the missing intermediate scales (100 pc to 1 kpc). The warped disk model suggests that there is a gap in the distribution at $6'' < r < 50''$, which is introduced ad-hoc in order to reproduce the observed lack of mid-IR emission between the long sides of the parallelogram filaments (Quillen et al. 2006), although it is not easy to distinguish whether this is just an inclination effect on the surface brightness of the dust emission. Our $^{12}\text{CO}(2-1)$ data, which is not affected by such effect, firmly show that there is still a lack of emission. If this model is correct, this would confirm the existence of the physical gap.

However, the warped disk model does not explain a number of deviations from our $^{12}\text{CO}(2-1)$ maps (§ 3.3), such as the brighter sides on the NW and SE of the parallel filaments. Furthermore, the P–V diagram along P.A. $\sim 135^\circ$ provides seemingly clear evidence that there are continuous layers of molecular gas from the innermost region in the SE to the outer disk (southern parallel filament), which is not in agreement with a gap within $6'' < r < 50''$ ($100 \text{ pc} < r < 800 \text{ pc}$) in the CO distribution as assumed in the warped disk model. Twin peaks in CO emission also seem to be observed into the nuclear region of Cen A (§ 3.3), which are usually detected in barred spiral galaxies (e.g. Kenney et al. 1992; Downes et al. 1996). Molecular gas, ionized gas and dust seem to be coextensive (§ 5). Most of the species show brighter emission to the NW and SE, rather than spread over the parallelogram-shaped structure. Overall, in a qualitative way, the presented contribution of a weak bar potential (see § 4.2, 4.3) reproduces the brighter emission of the NW and SE sides (§ 5) with enhanced SF, and naturally explains the formation of circumnuclear gas, its connection to gas at larger radii and a lack of emission along a preferential direction between the two. This weak bar could have originated in the merger event that brought the gas into the dust lane, and would efficiently help to funnel gas into the circumnuclear environment.

Note that this model is used just to illustrate the possible contribution of a weak bar model in Cen A. First, the pattern speed has been estimated by the unknown location of the IILR, which was set to the edge of the circumnuclear gas. Also, the model does not specify the distribution of orbit density (gas surface density) in the radial direction, and the gas distribution in the tangential direction is bisymmetric by definition even though many barred galaxies show deviations from it. And finally, the model is applicable only for infinitesimally weak bars. High resolution observations of CO transition lines along the whole dust lane will help to determine which model (or combination) is more likely. If confirmed that a weak

bi-symmetric potential is present in the central region of Cen A, one can wonder whether they could be one of the main drivers of activity, even in elliptical galaxies like Cen A. Otherwise one would have to argue that viscosity within the disk may be important to transport the gas toward the nuclear region (Duschl et al. 2000).

6.2. Relation between Molecular Gas Properties and Nuclear Activity

The gas-to-dynamical mass ratio and the degree of gas concentration toward the center are important parameters to know the star formation activity and the possible gas infall rate along a bar to a galactic center (e.g. Sakamoto et al. 1999). We compare these two properties for Cen A with the sample of spiral galaxies in Sakamoto et al. (1999). Sakamoto et al. (1999) set a limit of $r = 500$ pc between circumnuclear gas and outer gas. In order to compare with Sakamoto et al. (1999), we use a constant $X = 3.0 \times 10^{20} \text{ cm}^{-2} (\text{K km s}^{-1})^{-1}$ for both external and nuclear molecular gas. Although these two properties are affected by the uncertain X-factors as a function of radius within a galaxy, we assume that this source of error is similar for different galaxies, and thus the comparison still allows us to obtain meaningful results.

M_{gas} (gas mass) in the inner 500 pc and the surface density Σ_{gas} will also depend on how the molecular gas is distributed, which is different for each of the models explained in § 4. In case of the warped disk model, the gas mass and the surface density within 500 pc are $M_{\text{gas},500 \text{ pc}} \sim 6.1 \times 10^7 M_{\odot}$ and $\Sigma_{\text{gas},500 \text{ pc}} \sim 78 M_{\odot} \text{ pc}^{-2}$. In case of the weak bar models, most of the molecular gas detected with our observation is within the radius of 500 pc, so $M_{\text{gas},500 \text{ pc}} \sim 1.8 \times 10^8 M_{\odot}$ and $\Sigma_{\text{gas},500 \text{ pc}} \sim 230 M_{\odot} \text{ pc}^{-2}$.

The dynamical mass in the central 500 pc radius is calculated as $M_{\text{dyn},500 \text{ pc}} = r(v/\sin i)^2/G = 4.6 \times 10^9 M_{\odot}$, obtained from the maximum rotational velocity $v \simeq 200 \text{ km s}^{-1}$ and inclination of $i = 70^\circ$. The gas-to-dynamical mass ratio, $M_{\text{gas},500 \text{ pc}}/M_{\text{dyn},500 \text{ pc}}$, for the warped disk and the weak bar models can be calculated as 0.01 and 0.04, respectively. Both of these values show that the gas mass at the center of Cen A is only a few percent of the dynamical mass (See § 3.4). If we compare the results of Sakamoto et al. (1999), Cen A appears around the low end of their sample in either model. The galaxies with low gas-to-dynamical mass ratio in the Sakamoto et al. sample are dominated by Seyfert galaxies, and this is consistent with the existence of an AGN at the center of Cen A (although AGN activity is much higher in Cen A than in Seyferts). The low gas-to-dynamical mass ratio also suggests a low rate of star formation (Sakamoto et al. 1999), but it is inconsistent with the results by Wild & Eckart (2000), who find that the dense gas fraction $L_{\text{HCN}}/L_{\text{CO}}$ as well as the star formation efficiency $L_{\text{FIR}}/L_{\text{CO}}$ in the nuclear region of Cen A is comparable to ultra-luminous infrared galaxies (ULIRGs). This inconsistency may be, however, due to the effect of the AGN, not due to the star formation activities. Recent interferometric studies of Seyfert galaxies show that the HCN line is strongly enhanced toward the AGN dominated nuclei (e.g. Kohno et al. 2001; Kohno 2005). Dust around the nucleus can also be heated by the AGN, and it can enhance L_{FIR} . Future higher spatial resolution

CO and HCN observations, and comparisons with high resolution infrared data, will address this discrepancy.

To calculate the degree of gas concentration, we first calculate the gas surface density within the isophotal radius at 25 mag arcsec⁻², R_{25} , in B-band, following Sakamoto et al. (1999). Since this is an elliptical galaxy and the molecular gas is elongated along the minor axis, we take the R_{25} along the minor axis. In this case, $R_{25} = 10.0' = 10.0$ kpc. This yields $\Sigma_{\text{gas}, R_{25}} \sim 1.5 M_{\odot} \text{ pc}^{-2}$. The degree of gas concentration is therefore calculated as $f_{\text{con}} = \Sigma_{\text{gas}, 500 \text{ pc}} / \Sigma_{\text{gas}, R_{25}} \sim 52$ for the warped model and 150 for the weak bar models (~ 10 and ~ 30 respectively if a ratio of external to internal X factor of 5 is taken into account, see § 3.4). The value for the warped disk model is located at the high end of non-barred galaxies in the Sakamoto et al. sample, and that with the contribution of a weak bar model is located at the low end of barred galaxies. This result shows that the degree of gas concentration of Cen A in each of the models is consistent with the properties of disk galaxies which is surprising given the elliptical nature of Cen A, and probably that the concentration is not as extreme as in large-scale barred galaxies, as expected for a weak stellar potential proposed here.

7. SUMMARY AND CONCLUSIONS

We have observed the molecular gas as traced by the ¹²CO(2–1) line in the central 1 kpc of the nearby elliptical galaxy Cen A. The angular resolution achieved using the SMA is $6''.0 \times 2''.4$ (100 pc \times 40 pc). Our main findings are summarized as follows:

- We can distinguish between the following components: i) a rapidly rotating circumnuclear gas disk or torus (broad plateau component of the emission line) of 400 pc extent ($24''$), with a P.A. = 155° and perpendicular to the jet, and ii) molecular gas at larger radii associated with two apparently parallel filaments at a P.A. = 120° (narrow line component). The latter is observed to be coextensive with other components of the interstellar medium, such as the dust emission and PAHs from the $8\mu\text{m}$ mid-IR continuum emission, and is associated to the dust lane.
- We find the following signatures for non co-planar or non-circular motions: i) a large scale warp in the two parallel filaments, ii) brighter emission on the SE and NW sides in the two parallel filaments, iii) outer curvature in these filaments, iv) connections between the circumnuclear gas and that at larger radii, v) asymmetries in the distribution and kinematics in the circumnuclear gas. A twin peak CO emission line is probably observed in the circumnuclear gas. The P–V diagram shows a very steep rise

with $dv/dr = 19.2 \text{ km s}^{-1} \text{ arcsec}^{-1}$ within the inner 200 pc ($12''$), six times larger than in the outer component.

- We extend the currently prevalent warped-thin disk model in order to match the details in the inner kiloparsec of our ¹²CO(2–1) maps that still remained unexplained, in particular the contribution of the circumnuclear gas. However, deviations from this model include the brighter emission on the SE and NW sides in the two parallel filaments and the physical connection between the circumnuclear gas and that at larger radii. The contribution of a weak bar model is used to explain these deviations from the warped disk model. In addition to this, it naturally explains the rapidly rotating circumnuclear region, the observed connections between the outer gas and circumnuclear gas, and the gap feature between them. In this scenario the NW and SE sides of the filaments would be the shocks where larger concentrations of molecular gas are located, as well as enhanced SF as has been observed by other authors.
- We find a low gas-to-dynamical mass ratio, suggesting a low rate of star formation close to the AGN. The molecular gas concentration index $f_{\text{con}} = \Sigma_{\text{gas}, 500 \text{ pc}} / \Sigma_{\text{gas}, R_{25}} \sim 52$ for the warped model and 150 for the weak bar model. When compared with disk galaxies it is observed that the degree of gas concentration of Cen A (for both models) is consistent with the properties of disk galaxies which is surprising given the elliptical nature of Cen A.

We thank the SMA staff members who made the observations reported here possible. We especially acknowledge K. Sakamoto, P. T. P. Ho and L. Verdes-Montenegro for useful comments on the manuscript. We also thank A. Quillen for kindly making available the mid-IR images from Spitzer/IRAC and IRS and A. Sarma for the 21cm continuum data from VLA. This research has made use of NASA’s Astrophysics Data System Bibliographic Services, and has also made use of the NASA/IPAC Extragalactic Database (NED) which is operated by the Jet Propulsion Laboratory, California Institute of Technology, under contract with the National Aeronautics and Space Administration. This research was supported by a Marie Curie International Fellowship within the 6th European Community Framework Programme.

Facilities: SMA

REFERENCES

- Allen, C. W. 1973, *Astrophysical quantities* (London: University of London, Athlone Press, —c1973, 3rd ed.)
- Allen, M. G. et al. 2002, *ApJS*, 139, 411
- Antonucci, R. 1993, *ARA&A*, 31, 473
- Bland, J. 1986, PhD thesis, Univ. Sussex, (1986)
- Bland, J., Taylor, K., & Atherton, P. D. 1987, *MNRAS*, 228, 595
- Dame, T. M., Hartmann, D., & Thaddeus, P. 2001, *ApJ*, 547, 792
- de Vaucouleurs, G. et al. 1995, *VizieR Online Data Catalog*, 7155, 0
- Downes, D., Reynaud, D., Solomon, P. M., & Radford, S. J. E. 1996, *ApJ*, 461, 186
- Duschl, W. J., Strittmatter, P. A., & Biermann, P. L. 2000, *A&A*, 357, 1123
- Eckart, A. et al. 1990a, *ApJ*, 365, 522
- . 1990b, *ApJ*, 363, 451

- Eckart, A., Wild, W., & Ageorges, N. 1999, *ApJ*, 516, 769
- Espada, D., Peck, A. B., & Matsushita, S. 2008, (in prep.)
- Ferrarese, L. et al. 2007, *ApJ*, 654, 186
- Hardcastle, M. J. et al. 2003, *ApJ*, 593, 169
- Hawarden, T. G. et al. 1993, *MNRAS*, 260, 844
- Ho, P. T. P., Moran, J. M., & Lo, K. Y. 2004, *ApJ*, 616, L1
- Horiuchi, S., Meier, D. L., Preston, R. A., & Tingay, S. J. 2006, *PASJ*, 58, 211
- Israel, F. P. 1992, *A&A*, 265, 487
- . 1998, *A&A Rev.*, 8, 237
- Israel, F. P., Raban, D., Booth, R. S., & Rantakyro, F. T. 2008, *A&A*, 483, 741
- Israel, F. P., van Dishoeck, E. F., Baas, F., de Graauw, T., & Phillips, T. G. 1991, *A&A*, 245, L13
- Israel, F. P. et al. 1990, *A&A*, 227, 342
- Kenney, J. D. P., Wilson, C. D., Scoville, N. Z., Devereux, N. A., & Young, J. S. 1992, *ApJ*, 395, L79
- Kohno, K. 2005, in *American Institute of Physics Conference Series*, Vol. 783, *The Evolution of Starbursts*, ed. S. Hüttemeister, E. Manthey, D. Bomans, & K. Weis, 203–208
- Kohno, K., Kawabe, R., & Vila-Vilaró, B. 1999, *ApJ*, 511, 157
- Kohno, K. et al. 2001, in *Astronomical Society of the Pacific Conference Series*, Vol. 249, *The Central Kiloparsec of Starbursts and AGN: The La Palma Connection*, ed. J. H. Knapen, J. E. Beckman, I. Shlosman, & T. J. Mahoney, 672
- Kraft, R. P. et al. 2002, *ApJ*, 569, 54
- Krajnović, D., Sharp, R., & Thatte, N. 2007, *MNRAS*, 374, 385
- Leeuw, L. L., Hawarden, T. G., Matthews, H. E., Robson, E. I., & Eckart, A. 2002, *ApJ*, 565, 131
- Leon, S., Lim, J., Combes, F., & Dinh-v-Trung. 2003, in *Astronomical Society of the Pacific Conference Series*, Vol. 290, *Active Galactic Nuclei: From Central Engine to Host Galaxy*, ed. S. Collin, F. Combes, & I. Shlosman, 525
- Lim, J., Leon, S., Combes, F., & Dinh-v-Trung. 2003, in *Astronomical Society of the Pacific Conference Series*, Vol. 290, *Active Galactic Nuclei: From Central Engine to Host Galaxy*, ed. S. Collin, F. Combes, & I. Shlosman, 529
- Liszt, H. 2001, *A&A*, 371, 865
- Ma, C. et al. 1998, *AJ*, 116, 516
- Maloney, P., & Black, J. H. 1988, *ApJ*, 325, 389
- Marconi, A. et al. 2001, *ApJ*, 549, 915
- . 2006, *A&A*, 448, 921
- . 2000, *ApJ*, 528, 276
- Mauersberger, R., Henkel, C., Wielebinski, R., Wiklind, T., & Reuter, H.-P. 1996, *A&A*, 305, 421
- Mirabel, I. F. et al. 1999, *A&A*, 341, 667
- Moellenhoff, C., Hummel, E., & Bender, R. 1992, *A&A*, 255, 35
- Neumayer, N. et al. 2007, *ApJ*, 671, 1329
- Nicholson, R. A., Bland-Hawthorn, J., & Taylor, K. 1992, *ApJ*, 387, 503
- Phillips, T. G. et al. 1987, *ApJ*, 322, L73
- Quillen, A. C. et al. 2008, *MNRAS*, 384, 1469
- . 2006, *ApJ*, 645, 1092
- Quillen, A. C., de Zeeuw, P. T., Phinney, E. S., & Phillips, T. G. 1992, *ApJ*, 391, 121
- Quillen, A. C., Graham, J. R., & Frogel, J. A. 1993, *ApJ*, 412, 550
- Roberts, M. S. 1970, *ApJ*, 161, L9
- Rydbeck, G. et al. 1993, *A&A*, 270, L13
- Sakamoto, K., Okumura, S. K., Ishizuki, S., & Scoville, N. Z. 1999, *ApJS*, 124, 403
- Sarma, A. P., Troland, T. H., & Rupen, M. P. 2002, *ApJ*, 564, 696
- Sault, R. J., Teuben, P. J., & Wright, M. C. H. 1995, in *ASP Conf. Ser. 77: Astronomical Data Analysis Software and Systems IV*, ed. R. A. Shaw, H. E. Payne, & J. J. E. Hayes, 433
- Schiminovich, D., van Gorkom, J. H., van der Hulst, J. M., & Kasow, S. 1994, *ApJ*, 423, L101
- Schmitt, H. R., Pringle, J. E., Clarke, C. J., & Kinney, A. L. 2002, *ApJ*, 575, 150
- Schreier, E. J., Koekemoer, A., & Marconi, A. 1998a, in *Abstracts of the 19th Texas Symposium on Relativistic Astrophysics and Cosmology*, held in Paris, France, Dec. 14-18, 1998. Eds.: J. Paul, T. Montmerle, and E. Aubourg (CEA Saclay), meeting abstract., ed. J. Paul, T. Montmerle, & E. Aubourg
- Schreier, E. J. et al. 1998b, *ApJ*, 499, L143
- Tingay, S. J. et al. 1998, *AJ*, 115, 960
- Ulvestad, J. S., & Wilson, A. S. 1984, *ApJ*, 285, 439
- van der Hulst, J. M., Golisch, W. F., & Haschick, A. D. 1983, *ApJ*, 264, L37
- van Gorkom, J. H., van der Hulst, J. M., Haschick, A. D., & Tubbs, A. D. 1990, *AJ*, 99, 1781
- Verdoes Kleijn, G. A., & de Zeeuw, P. T. 2005, *A&A*, 435, 43
- Wada, K. 1994, *PASJ*, 46, 165
- Weiß, A., Neininger, N., Hüttemeister, S., & Klein, U. 2001, *A&A*, 365, 571
- Wiklind, T., & Combes, F. 1997, *A&A*, 324, 51
- Wild, W., & Eckart, A. 2000, *A&A*, 359, 483
- Wilson, C. D. 1995, *ApJ*, 448, L97

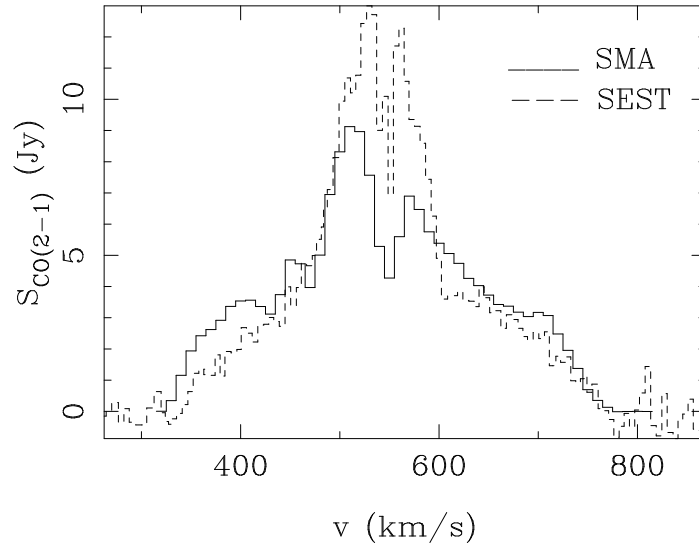


FIG. 1.— Comparison of the SEST spectrum from Israel (1992, ; dashed line) with that obtained by us using the SMA (solid line) and convolved to the $23''$ beam of the SEST. Note that the high velocity wings (300 to 500 km s^{-1} and 600 to 800 km s^{-1}) show good agreement, while we miss some flux in the narrow line (500 km s^{-1} to 600 km s^{-1}). The small deviation in the broad plateau is probably due to a slightly wrong baseline subtraction in the single-dish data.

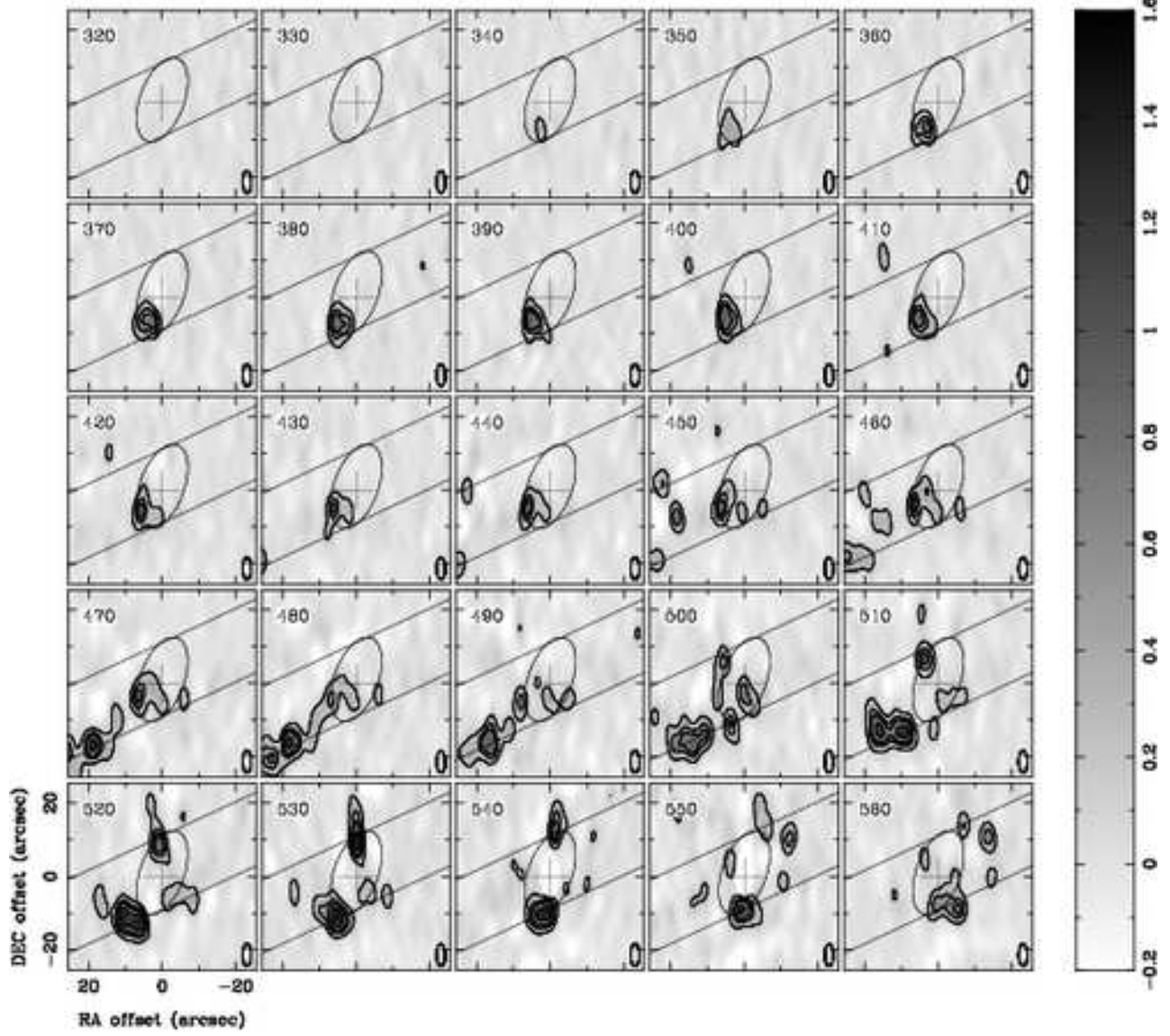


FIG. 2.— Channel map of the $^{12}\text{CO}(2-1)$ line of Cen A, made using uniform weighting, in the LSR velocity range $V = 320 - 810 \text{ km s}^{-1}$ in 10 km s^{-1} bins. The velocities are shown in the upper left corner and the synthesized beam is shown in the lower right corner of each panel. The rms noise of an individual channel is 64 mJy beam^{-1} . The contour levels are 3, 7, 16 and 25σ (which corresponds to 0.19, 0.44, 1.02 and $1.60 \text{ Jy beam}^{-1}$). The cross sign shows the position of the AGN: R.A. = $13^{\text{h}}25^{\text{m}}27.^{\text{s}}615$; Dec. = $-43^{\circ}01'08''.805$ (Ma et al. 1998). The central ellipse indicates the location of the resolved inner circumnuclear component, and the two parallel lines the location of the molecular gas associated with the dust lane (narrow line component). Note that the P.A. of the major axis of the ellipse (P.A. $\simeq 155^{\circ}$) is different from that of the gas at larger radii (P.A. $\simeq 120^{\circ}$). Absorption features are found toward the galactic center, which are apparent in our maps in the $540 - 550 \text{ km s}^{-1}$ channels but are also present up to about 625 km s^{-1} (Espada et al. 2008).

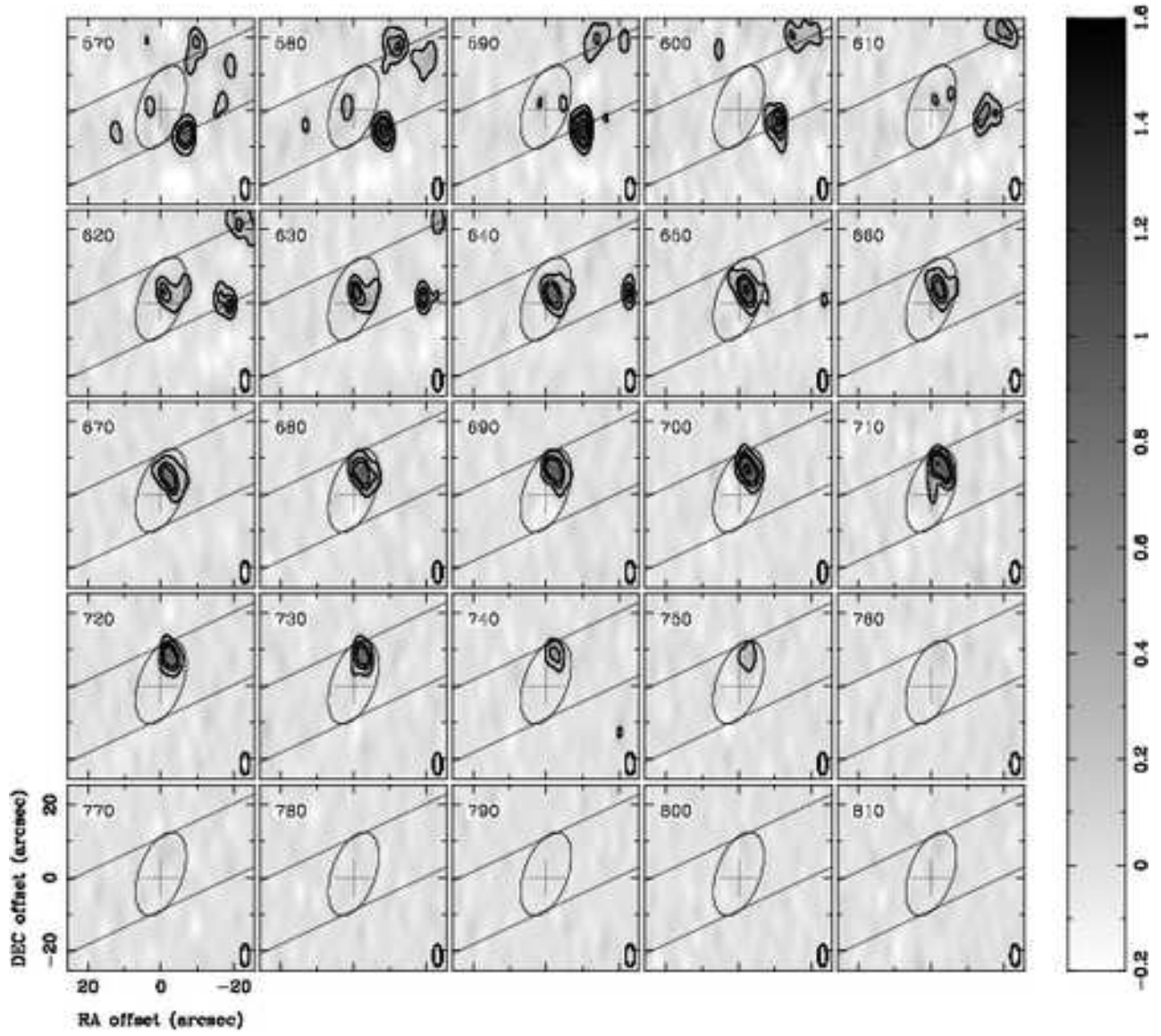


FIG. 2.— Continued.

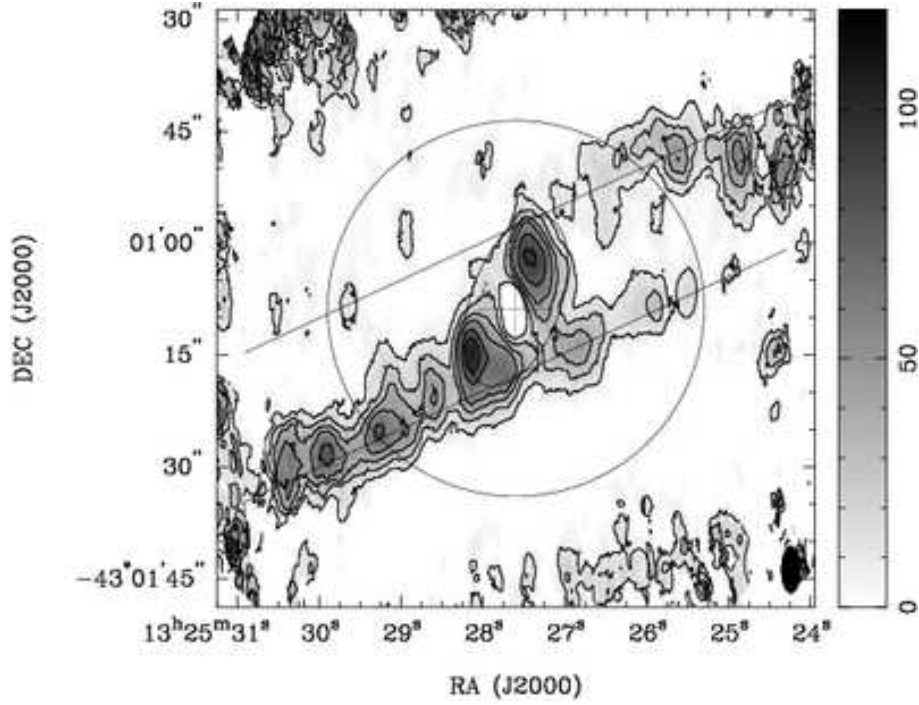


FIG. 3.— $^{12}\text{CO}(2-1)$ integrated intensity map in Cen A. Primary beam correction was performed in this image, as emission was found beyond the $52''$ full half power width of the primary beam (circle). Contour levels are 22.5, 36, 49.5, 72, 90 and 112.5 $\text{Jy beam}^{-1} \text{km s}^{-1}$. The synthesized beam ($2''.4 \times 6''.0$) is indicated by a filled ellipse in the lower corner of the plot, and the colour scale for the $^{12}\text{CO}(2-1)$ intensity is shown beside the plot in $\text{Jy beam}^{-1} \text{km s}^{-1}$. For the central ellipse, the cross, and the two lines, see Figure 2.

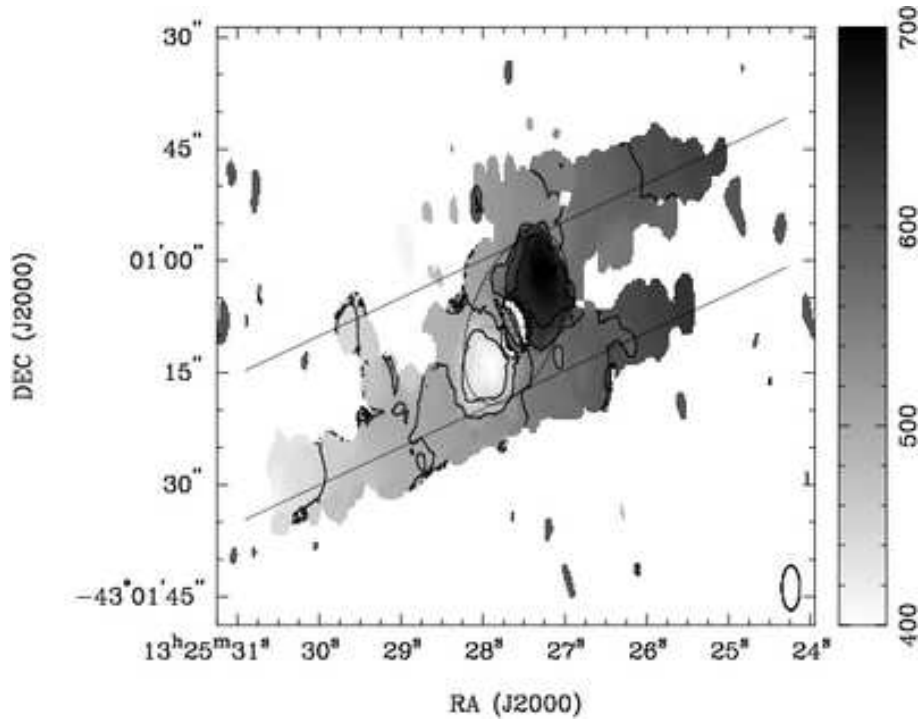


FIG. 4.— $^{12}\text{CO}(2-1)$ (intensity weighted) velocity field map of Cen A. Contours are placed every 50 km s^{-1} , from 425 – 675 km s^{-1} . The color scale ranges from 400 km s^{-1} up to 700 km s^{-1} . The size of the synthesized beam is shown in the lower right corner. For the central ellipse, the cross, and the two lines, see Figure 2.

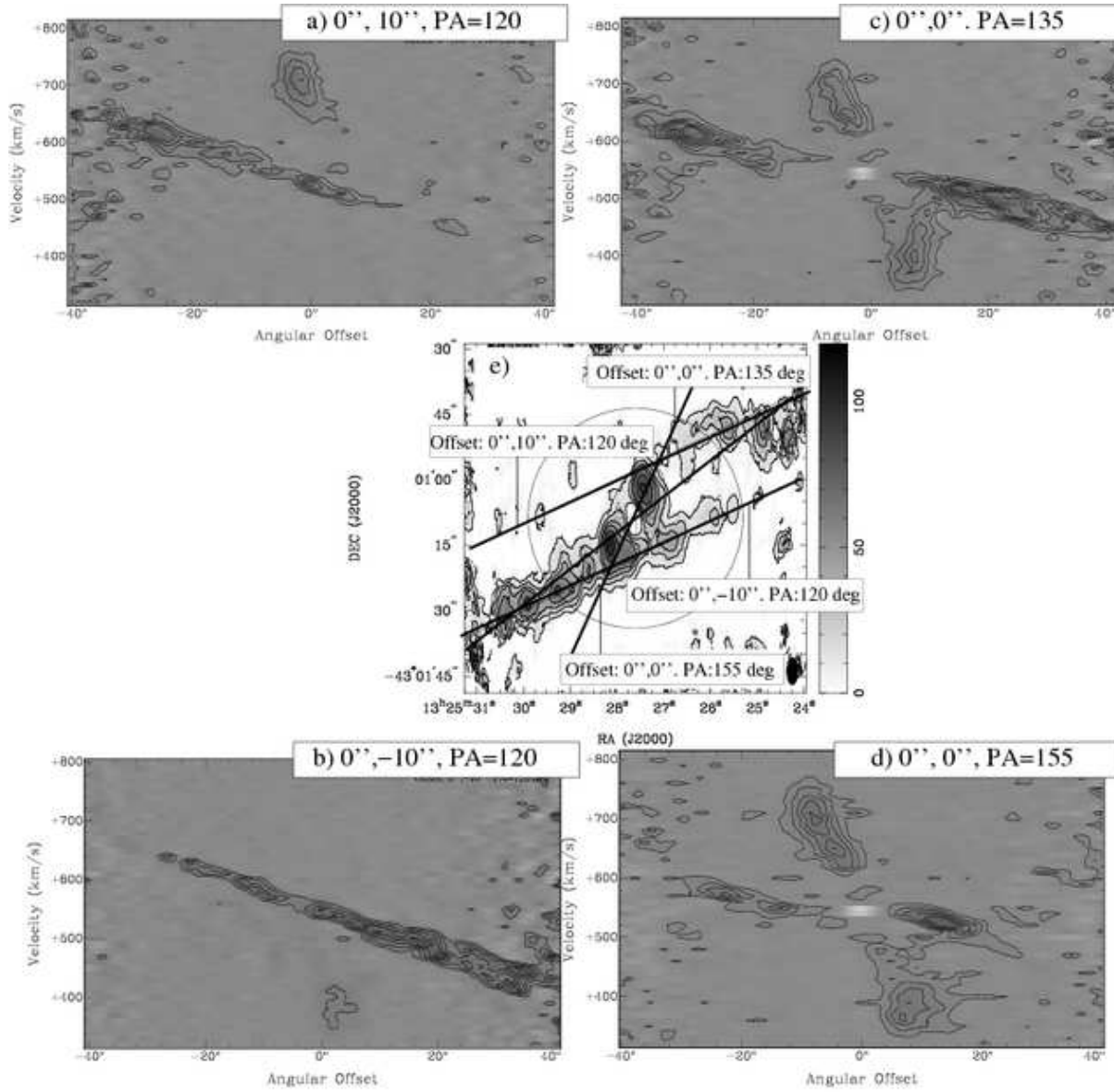


FIG. 5.— a) – b) Position–Velocity (P–V) diagrams at 120° (dust lane major axis) with an offset of $\pm 10''$ in Dec., with contour levels 0.5, 0.9, 1.3, 1.7 and 2.1 Jy beam^{-1} .) c) – d) P–V diagrams at P.A. = 135° and 155° (circumnuclear gas major axis), both centered in the AGN. Contour levels are: 0.4, 0.7, 0.9, 1.2, 1.5 and 1.8 Jy beam^{-1} . e) Plot showing the different P–V cuts over the $^{12}\text{CO}(2-1)$ integrated intensity map. Positive angular offsets are given for the SE, negative for the NW.

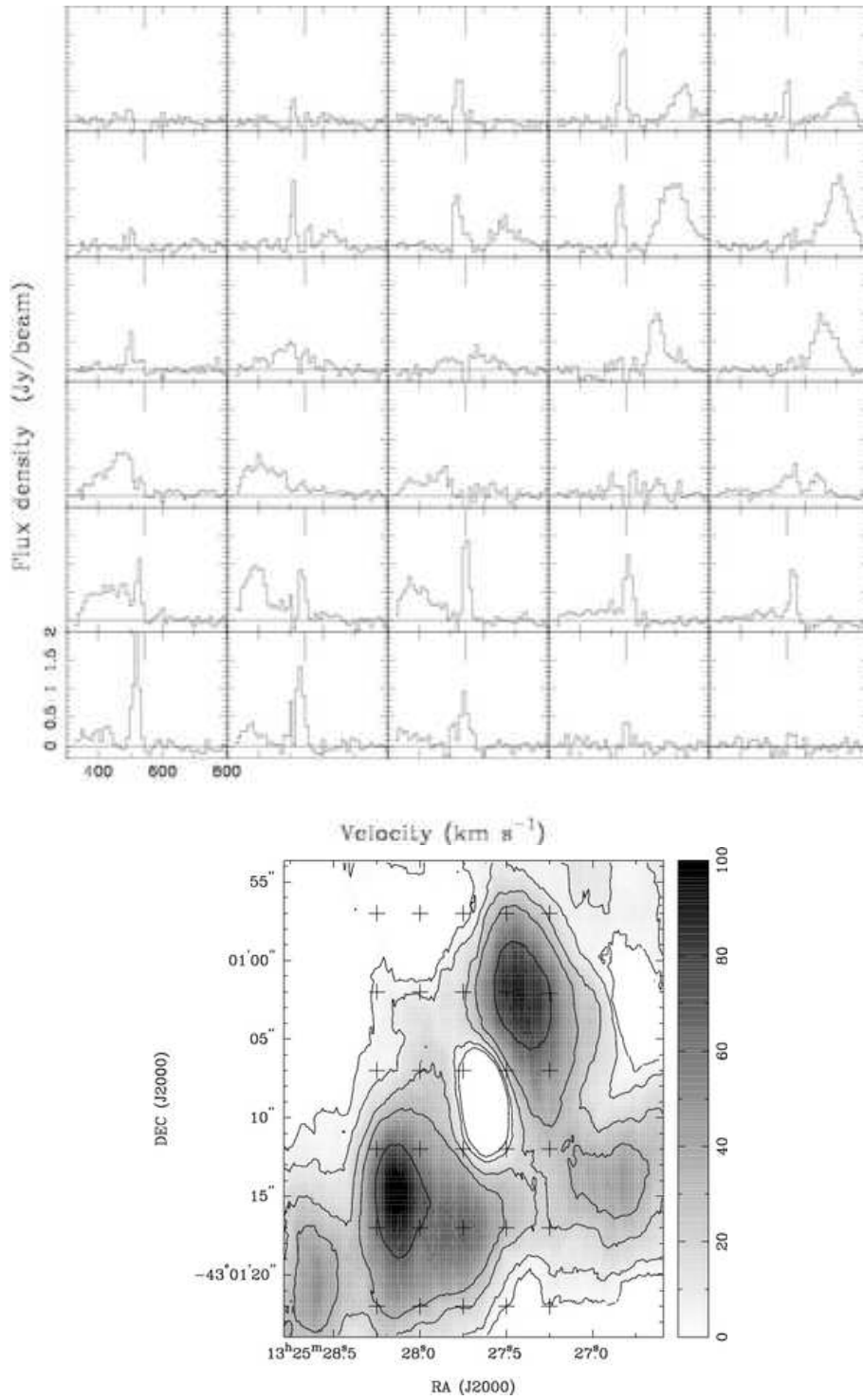


FIG. 6.— a) $^{12}\text{CO}(2-1)$ line profiles on a 5×6 grid with spacings $0^{\text{s}}25$ in R.A. and $5''$ in Dec., covering the circumnuclear disk and part of the outer molecular gas. The flux density of the profiles spans from 0 to 2 Jy beam $^{-1}$, and the x-axis shows velocity from 320 to 810 km s $^{-1}$ with 10 km s $^{-1}$ resolution. b) Integrated $^{12}\text{CO}(2-1)$ flux densities map (see Figure 3). Cross marks the grid positions shown in Figure a).

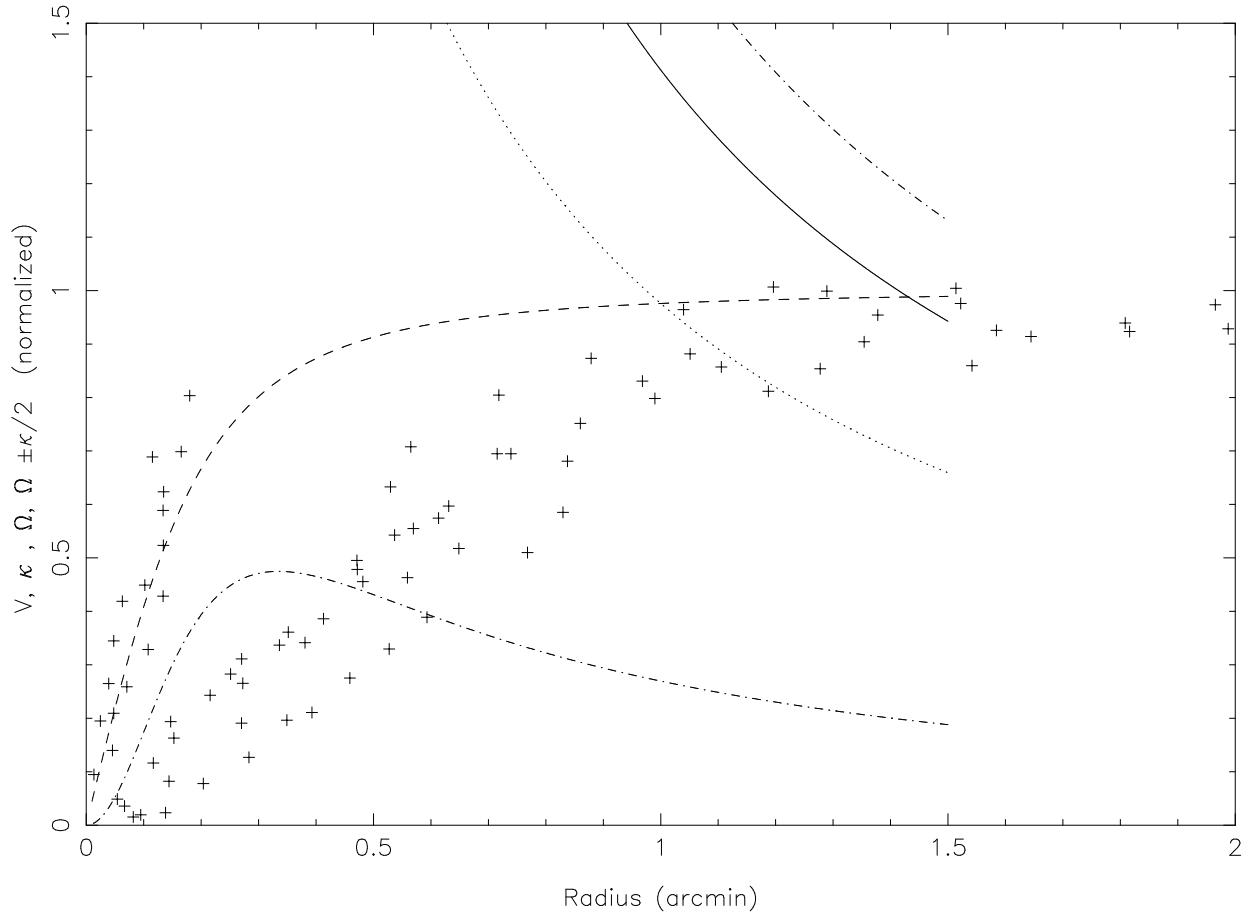


FIG. 7.— Rotation curve (dashed line) roughly estimated using line of sight velocity data (cross signs) of $^{12}\text{CO}(2-1)$ in the high velocity circumnuclear gas up to $r = 200$ pc ($12''$, this work), $^{12}\text{CO}(2-1)$ in the outer regions (this work), $\text{H}\alpha$ (Nicholson et al. 1992) and $^{12}\text{CO}(3-2)$ (Liszt 2001). Data points are obtained from the derived line of nodes or directly from the position velocity diagrams, overlapping both the receding and approaching sides, divided by $V = 260 \text{ km s}^{-1}$, which corresponds to its maximum. The bimodality of the inner data points corresponds to the nuclear and outer gas. A reasonable fit which suffice to qualitatively model the nuclear region of the galaxy is obtained using an axisymmetric logarithmic potential $\Phi_0(r) = 0.5 \times \log(a + (r^2)/b)$, with $a = 1.0$ and $b = 0.05$. Ω (full line), κ (dotted line) and $\Omega \pm \frac{\kappa}{2}$ (dashed-dotted lines) are also shown. This is the generic curve used in the tilted-ring, weak bar and weak bar+tilted-ring models shown in Figure 8, 10 and 11.

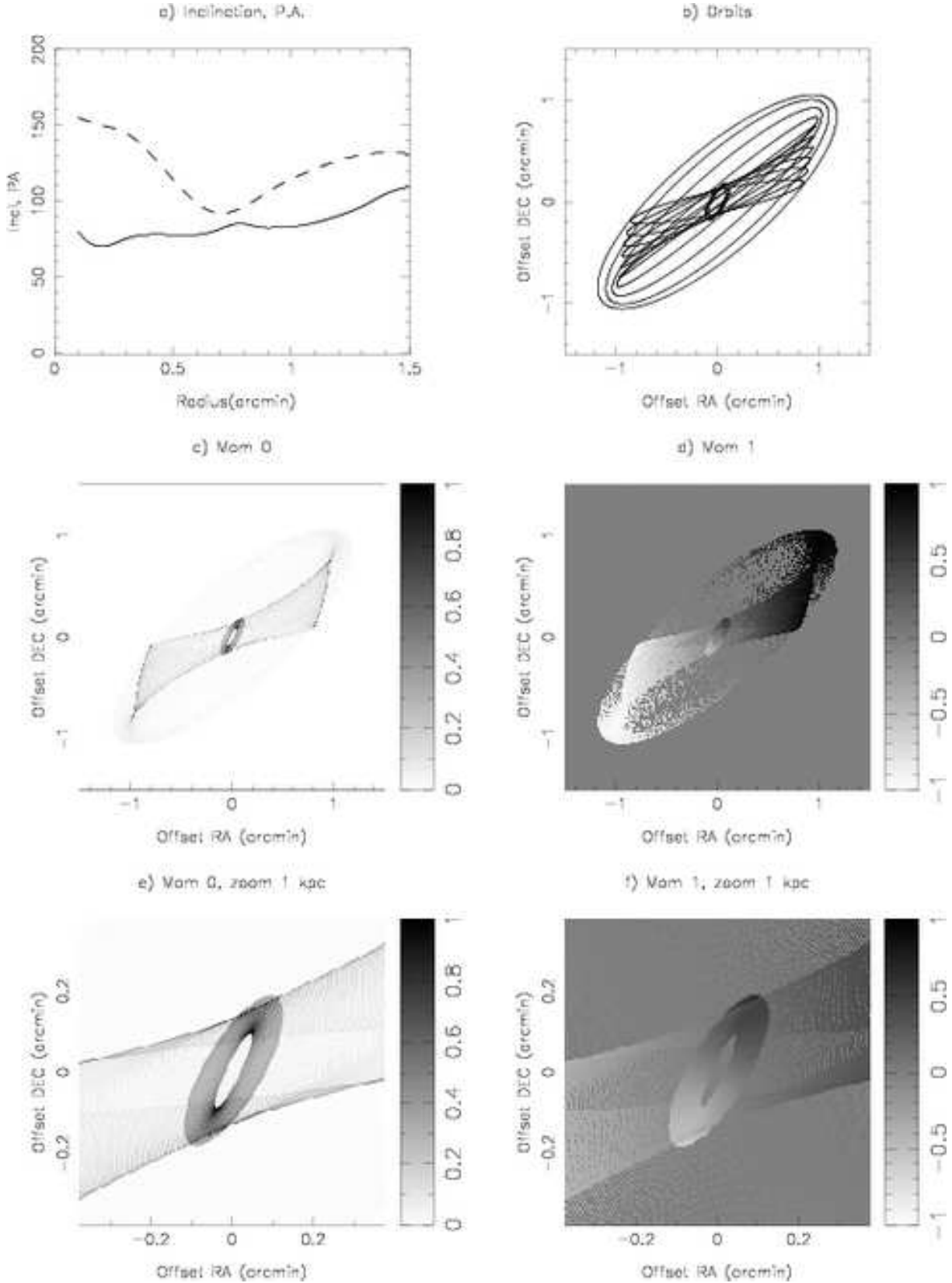


FIG. 8.— Warped thin disk model (§ 4.1): a) Inclination (solid line) and P.A. (dashed line) as a function of radius in arcmin for the warped disk analysis, b) projected orbits, c) and d) distribution and velocity field for a field of view of 4 kpc ($250''$), e) and f) distribution and velocity field for a smaller field of view of 1 kpc ($62''$). The intensity has been normalized so that its maximum is unity. We use the rotation curve as shown in Figure 7. Inclination and P.A. are the same as in Quillen et al. (2006). We model a circumnuclear disk within radii $r < 0.2$ kpc as suggested by our observations. The gap up to $r = 0.8$ kpc is required in this model in order to remove a bright linear feature within the parallelogram structure (Quillen et al. 2006, Figure 10).

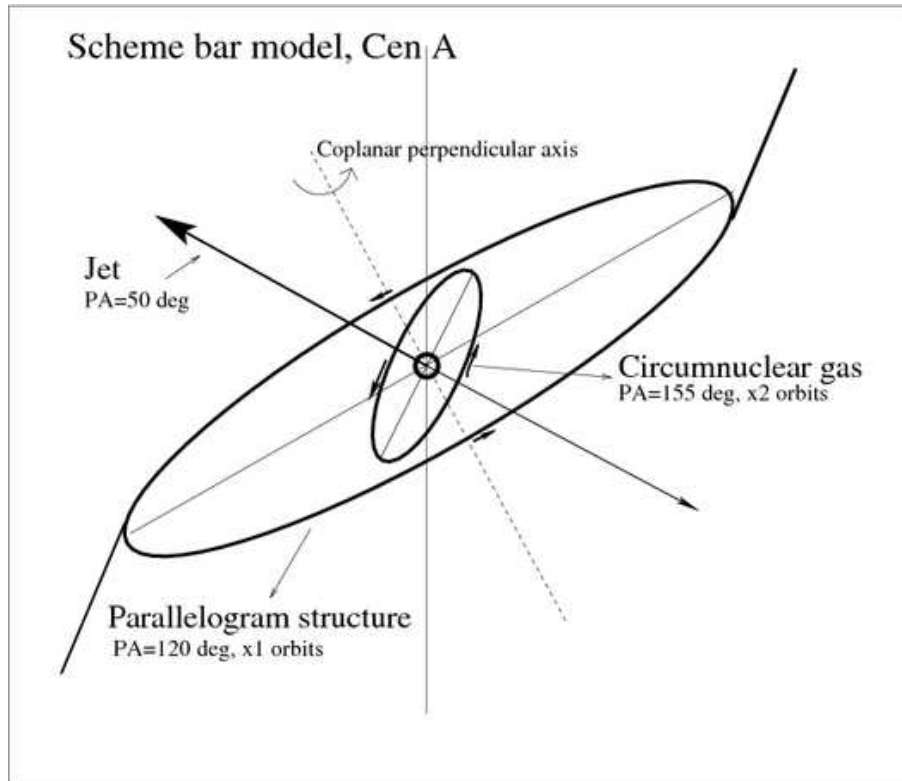


FIG. 9.— Scheme illustrating all the components present in the inner 3 kpc of Cen A in the proposed weak bar model scenario.

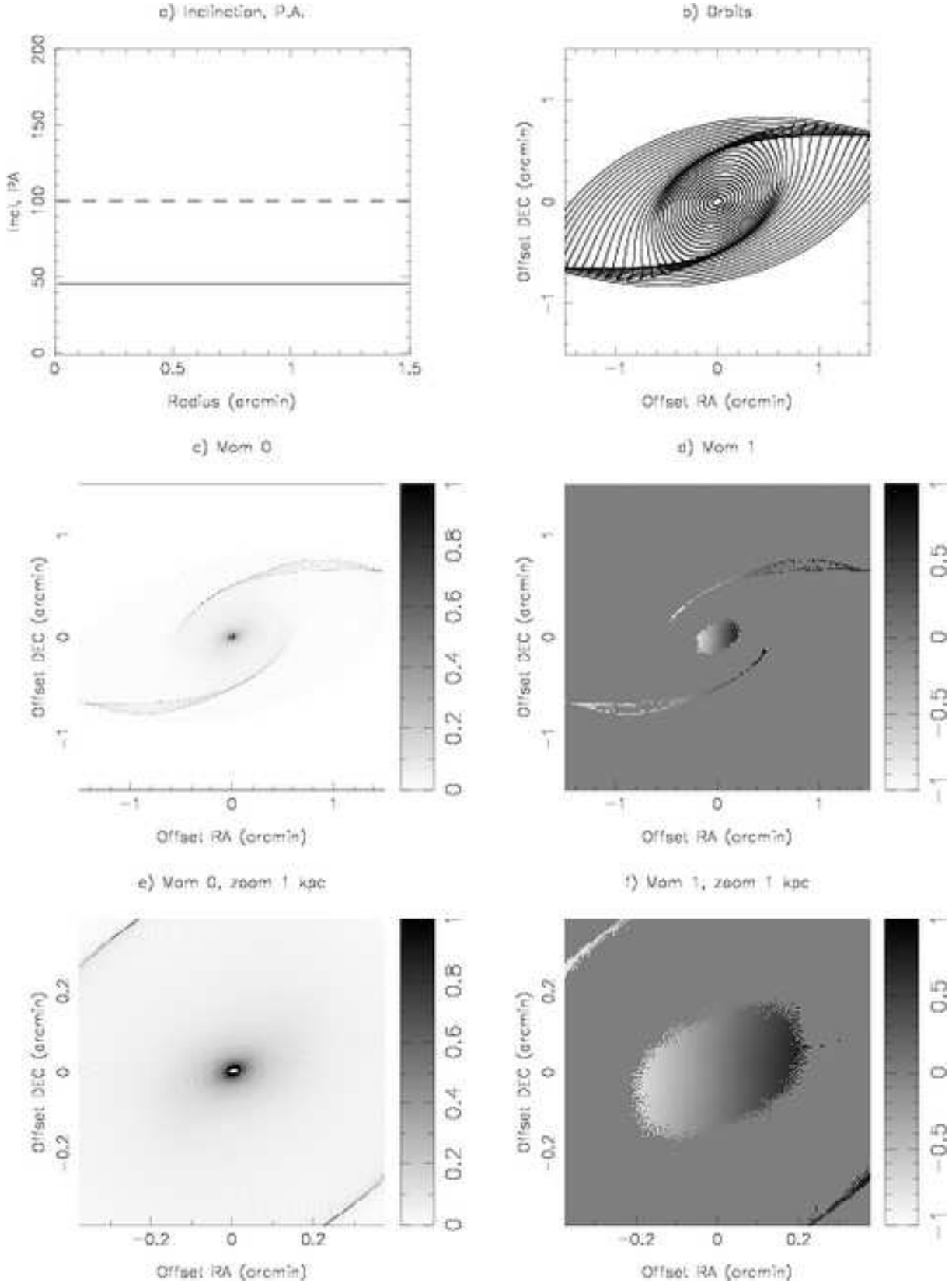


FIG. 10.— Co-planar weak bar model (§ 4.2). Plots are as in Figure 8, but here we simulate that the gas distribution is co-planar and non-circular motions using a weak bar model. Inclination and P.A. are kept constant to 45° and 100° . Note that a lower inclination to the actual $i \simeq 70^\circ$ is used in order to better illustrate the appearance of the spiral arms, circumnuclear disk as well as a preferential direction with lack of emission. The model follows the formalism in Wada (1994). Bar potential is $\Phi_0(r) = 0.5 \times \epsilon \log(a + r^2/b)$, with $a = 1.0$ and $b = 0.05$, which roughly fits the estimated rotation curve shown in Figure 7. We fixed $\Omega_b = 0.3$, $\epsilon = 0.03$ and $\Lambda = 0.1$.

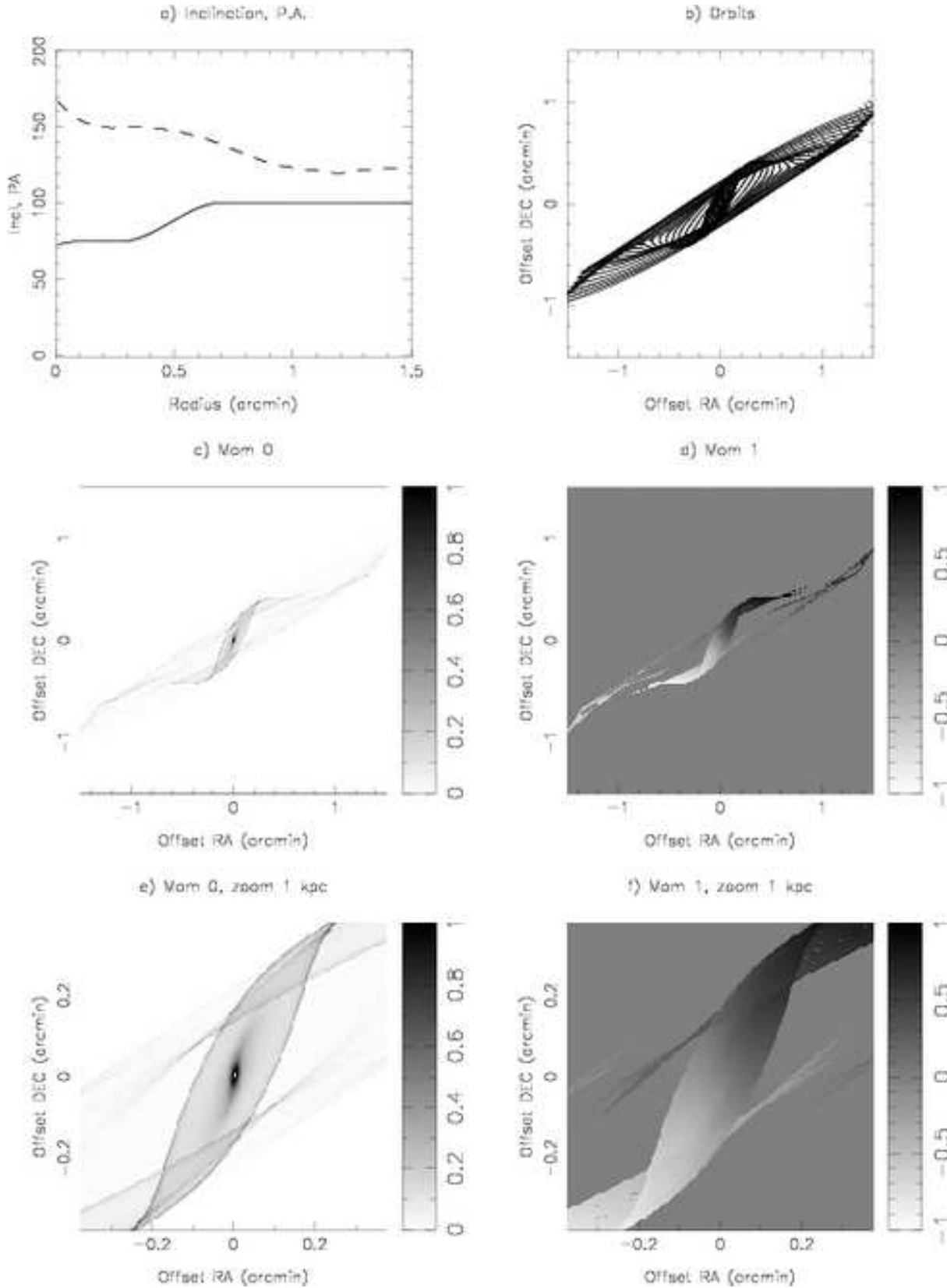


FIG. 11.— Bar + warped disk model (§ 4.3): as in Figure 10, we fixed $\Omega_b = 0.3$, $\epsilon = 0.03$ and $\Lambda = 0.10$, but this time slightly varying inclination and P.A. as a function of radius. Two main constraints have been taken into account: i) P.A. from 155° (our circumnuclear gas region) to 120° (parallelogram filaments, dust lane); b) Inclination from $i \geq 70^\circ$ for the circumnuclear gas (§ 3) with near side to the SW, to $i \simeq 70 - 80^\circ$ with opposite near side for the gas at larger radii (indicated with values $100 - 110^\circ$ in Fig. 11 a). The rotation curve used is shown in Figure 7.

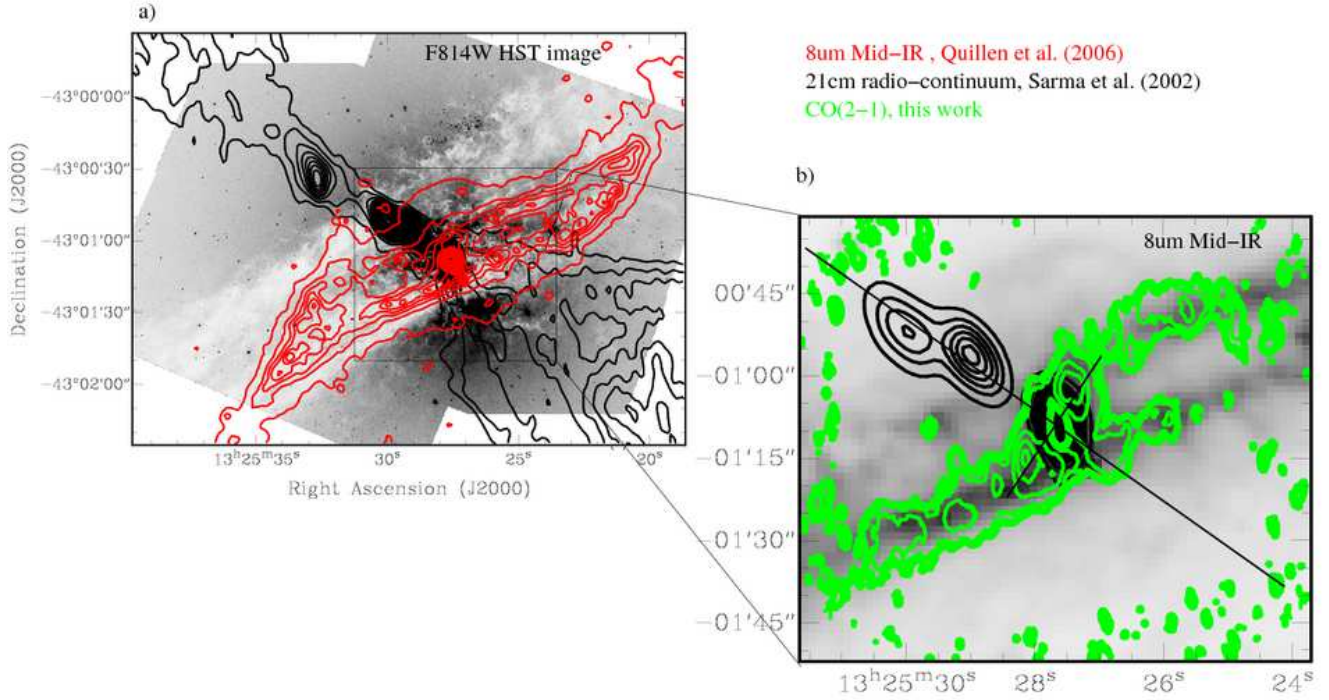


FIG. 12.— Comparison of the dust lane location, ($8\ \mu\text{m}$) dust emission distribution (Quillen et al. 2006), $^{12}\text{CO}(2-1)$ emission (this work) and the 21cm radio-continuum jet (Sarma et al. 2002). a) HST I analog filter F814W image (Schreier et al. 1998a; lighter values show location of the dust lane), and superposed the Spitzer mid-IR $8\ \mu\text{m}$ emission in red contours (Quillen et al. 2006; FWHM of the PSF is $2''.0$ and the rms of the mid-IR image is $0.06\ \text{MJy sr}^{-1}$ in steps of $30\ \text{MJy sr}^{-1}$) and 21cm radio continuum emission in black contours (Sarma et al. 2002; Figure 1a., nucleus and inner lobes, the beam is $8''.4 \times 4''.2$ and the rms in the image is $9\ \text{mJy beam}^{-1}$ in steps of $90\ \text{mJy beam}^{-1}$). b) Mid-IR $8\ \mu\text{m}$ image from Spitzer this time in grey scale (minimum is -0.06 and maximum $974.84\ \text{MJy sr}^{-1}$). Black contours show Sarma et al.'s radio continuum (from $0.4\ \text{Jy beam}^{-1}$ to 6.0 in steps of $0.4\ \text{Jy beam}^{-1}$) and the green contours the $^{12}\text{CO}(2-1)$ distribution (this work, same contours as in Fig. 2). Note the clear correspondence between the main clumps of $^{12}\text{CO}(2-1)$ and mid-IR $8\ \mu\text{m}$ emission and that the jet is nearly perpendicular to the circumnuclear molecular gas.

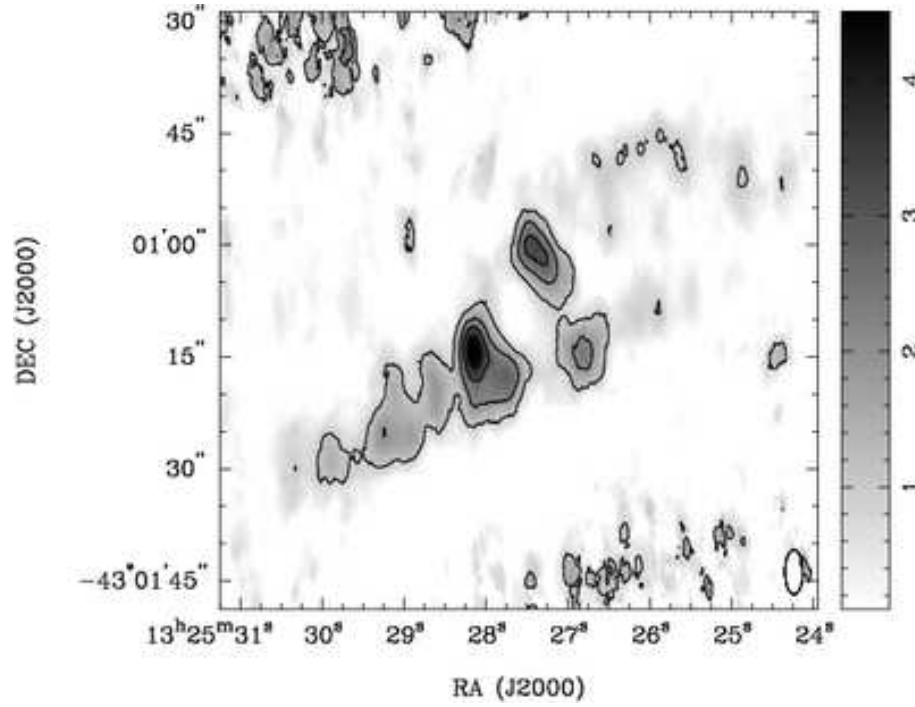


FIG. 13.— Ratio of integrated flux densities between the $^{12}\text{CO}(2-1)$ (as in Fig. 3) and the mid-IR Spitzer $8\ \mu\text{m}$ (as in Fig.12 b but convolved with a $6''.0 \times 2''.4$ beam), and divided by 30. Contours are at 1, 2, 3 and 4 (dimensionless since we set both in units of Jy beam^{-1}).

TABLE 1
GENERAL PROPERTIES OF CENTAURUS A (NGC 5128)

Morphology ^a	E2, peculiar
R.A. (J2000) ^b	13 ^h 25 ^m 27 ^s .615
Decl. (J2000) ^b	-43°01'08''805
Distance (Mpc) ^c	3.42 ± 0.18 (random) ± 0.25 (systematic)
Linear scale ("/>pc)	16.5
D_{25} (') ^d	25.7
d_{25} (') ^d	20.0
V_{LSR} (km s ⁻¹) ^a	543 ± 2
L_{B} , blue luminosity (L_{\odot}) ^e	3.45×10^{10}
M_{HI} (M_{\odot}) ^a	$(8.3 \pm 2.5) \times 10^8$
M_{H_2} (M_{\odot}) ^e	3.4×10^8
L_{FIR} (L_{\odot}) ^f	$(0.6 - 1.8) \times 10^9$

^aIsrael (1998)

^bMa et al. (1998), VLBI observations at 2.3/8.4 GHz

^cFerrarese et al. (2007), distance calculated using cepheids.

^dde Vaucouleurs et al. (1995)

^eEckart et al. (1990b)

^fWild & Eckart (2000), range indicates the average value over the large scale disk as well as in the nuclear region $r < 1$ kpc.

TABLE 2
MAIN PARAMETERS OF THE ¹²CO(2-1) SMA OBSERVATIONS

Date	2006 April 5
Configuration	7 antennas, Compact N-S unprojected baselines: 16 – 70 m projected baselines: 6 – 30 m
R.A. of phase center (J2000)	13 ^h 25 ^m 27 ^s .6
Decl. of phase center (J2000)	-43°01'09''0
Time on source (hr)	2
FWHM of primary beam	52''
FWHM of synthesized beam	2''.4 × 6''.0 (40 × 100 pc), P.A. = 0°
Velocity at band center (km s ⁻¹)	550
Total bandwidth	2 GHz in each sideband (about 2800 km s ⁻¹) (separated by 10 GHz)
rms noise (10 km s ⁻¹)	0.064 Jy beam ⁻¹
Spectral resolution (km s ⁻¹)	1 km s ⁻¹

TABLE 3
DERIVED PARAMETERS OF THE ¹²CO(2-1) EMISSION LINES

Component	Peak Flux Density (Jy beam ⁻¹ km s ⁻¹)	Mean Vel. (km s ⁻¹)	Vel. Width (km s ⁻¹)	$S_{12\text{CO}(2-1)}$ (Jy km s ⁻¹)	M_{H_2} (M_{\odot})
Broad line (Circumnuclear gas)	126 ± 1	560 ± 15	314 ± 15	1182 ± 5	$(0.6 \pm 0.1) \times 10^7$
Narrow line (Outer gas)		535 ± 15	160 ± 15	2324 ± 14	$(5.9 \pm 0.3) \times 10^7$
All				3506 ± 15	$(6.5 \pm 0.3) \times 10^7$

NOTE. — We adopt a galactic CO-to-H₂ conversion factor $X = 0.4 \times 10^{20} \text{ cm}^{-2} (\text{K km s}^{-1})^{-1}$ for the circumnuclear gas and $X = 2.0 \times 10^{20} \text{ cm}^{-2} (\text{K km s}^{-1})^{-1}$ for the outer gas, estimated following recent values for X for our own galaxy as a function of radius (Dame et al. 2001). We use equations in §. 4 of Sakamoto et al. (1999) for molecular gas mass M_{H_2} and gas surface density Σ_{gas} using $M_{\text{gas}} = 1.36 M_{\text{H}_2}$, where the factor 1.36 accounts for elements other than hydrogen (Allen 1973).

TABLE 4
LINE OF SIGHT VELOCITY CURVE

Position range (pc ($''$))	Velocity gradient (dv/dr) ($\text{km s}^{-1} \text{pc}^{-1}$)	Resolution ($''$)	Line	Comment
80 – 165 (5 – 10)	1.2	6.0×2.4	$^{12}\text{CO}(2-1)^{\text{a}}$	Circumnuclear gas
80 – 335 (5 – 20)	0.2	6.0×2.4	$^{12}\text{CO}(2-1)^{\text{a}}$	Outer molecular gas
30 – 3000 (2 – 180)	0.3	2×2	$\text{H}\alpha^{\text{b}}$	Up to 1 kpc, then flat
750 – 2500 (45 – 150)	0.2	45×45	$^{12}\text{CO}(1-0)^{\text{c}}$	Up to 1.5 kpc
235 – 835 (14 – 50)	0.2	14×14	$^{12}\text{CO}(3-2)^{\text{d}}$	Outer molecular gas
1000 – 5000 (60 – 300)	$\simeq 0.1$	77×33	H I^{e}	Up to 2 kpc

^aThis work

^bNicholson et al. (1992)

^cEckart et al. (1990b)

^dLiszt (2001)

^evan Gorkom et al. (1990)